Path-integral molecular dynamics predictions of equilibrium H and O isotope fractionations between brucite and water

Caihong Gao [a], Yining Zhang [a], Qi Liu [a], Yuhong Yang [a,b], Yun Liu [a,b,c,*]

[a] *State Key Laboratory of Ore Deposit Geochemistry, Institute of Geochemistry, Chinese Academy of Sciences, Guiyang 550081, China*
[b] *International Center for Planetary Science, College of Earth Sciences, Chengdu University of Technology, Chengdu 610059, China*
[c] *CAS Center for Excellence in Comparative Planetology, Hefei 230026, China*

A B S T R A C T

Precise prediction of hydrogen (H) isotope fractionations among different substances is a long-standing challenge in isotope geochemistry, as it needs treatments beyond the harmonic approximation. Path-integral molecular dynamics (PIMD) simulations have recently been proved to be valid in predicting equilibrium isotope fractionations for light elements. However, the lack of reliable force fields hinders the application of PIMD to the condensed phases. In this work, the deep potential models trained on the first-principles molecular dynamics (FPMD) data are applied to PIMD simulations to determine the D/H and $^{18}O/^{16}O$ isotope fractionation factors between brucite and water. To quantitatively assess the influence of quantum effects, the D/H and $^{18}O/^{16}O$ isotope fractionations between brucite and water are also determined under the framework of harmonic approximation.

By comparing the results of the PIMD and those of harmonic calculations, we find that H and O atoms in brucite and water are strongly affected by the anharmonic effects. The accuracy of the harmonic isotope fractionations mainly depends on the cancellation percentage of the anharmonic effects on the reduced partition function ratios (RPFRs) of the two substances. The isotope fractionations predicted by PIMD simulations are close to the experimental results at high temperatures. However, at low temperatures, the predicted isotope fractionations are different from those of experiments. The discrepancies are attributed to the approximations in the density functional theory (DFT) functionals used in this work, i.e., the inaccuracy in predicting the proton positions in brucite and water. Moreover, we find that the H isotope fractionations are extremely sensitive to the change of pressure. The direction of H isotope fractionation between brucite and water (at 300 K) will be even inversed as the pressure increases to more than 3 GPa. This strong pressure sensitivity may be a common characteristic of hydrous minerals and water systems. Therefore, the extrapolated H isotope fractionations used in the studies of dehydration of subducting slabs or deep Earth H distribution based on the isotope fractionations under low pressures may need to be rechecked.

1. Introduction

Serpentinization is one of the most important rock-water reactions in geosciences. The possible water cycling between the mantle and the Earth's surface largely depends on this reaction since the emergence of the hydrosphere of Earth. Brucite, the mineral form of $Mg(OH)_2$, mainly occurs as a secondary mineral in the serpentinization zones of altered ultramafic rocks (e.g., Hostetler et al., 1966; Page, 1967; Neal and Stanger, 1984; D'Antonio and Kristensen, 2004) and as an alteration product of periclase in the dolomites and limestones (e.g., Tilley, 1947; Alabaster, 1977; Nakajima et al., 1992; Bowles et al., 2011). It has a relatively simple octahedral structure and is considered to be a good analog for the octahedral sheet of Mg-bearing phyllosilicates. The presence of H and O in its crystal lattice makes it one of the most important hydrous minerals in the lithosphere. Thus, knowing the isotope fractionations between brucite and the aqueous fluids is particularly important because it could shed light upon the origin of isotope variations during the alteration process of silicate rocks and the dehydration process of hydrous minerals.

Recent experimental works have reported the D/H isotope fractionation factors between brucite and water at various temperatures and pressures (e.g., Satake and Matsuo, 1984; Saccocia

---

et al., 1998; Xu and Zheng, 1999; Horita et al., 1999; 2002; 2018), but significant discrepancies exist among some of these works. For example, Satake and Matsuo (1984) applied the partial exchange method (Northrop and Clayton, 1966) to determine the D/H isotope fractionations between brucite and water at 100–510 °C and reported a relatively narrow range of fractionations (−26.9‰ to −33.9‰). These values are close to the results of later experiments (Saccocia et al., 1998; Horita et al., 2002; 2018), but are significantly larger than the isotope fractionations (−57‰ to −78‰) determined by Xu and Zheng (1999) at 25–100 °C. The D/H isotope fractionations between brucite and water are found to be related to the dissolved NaCl in the aqueous solutions and the pressure of the experiments (Saccocia et al., 1998; Horita et al., 1999; 2002; 2018), but these effects failed to explain the large discrepancy at temperatures around 100 °C. For O isotopes, Saccocia et al. (1998) experimentally found that brucite is depleted in ^{18}O relative to NaCl solutions at 250–450 °C. Xu and Zheng (1999) reported an inversion of oxygen isotope fractionations between brucite and water at 60 °C. Together with previous experimental results, Saccocia et al. (2015) obtained a smooth function of $10^3\ln(\alpha_O)$ – temperature valid from 15 to 450 °C.

Accurate prediction of H isotope fractionation at different conditions is a long-term problem in the field. Theoretical studies based on the density functional theory (DFT) seldom reproduce the experimental H and O isotope fractionations between brucite and water. Instead, additional corrections were used to improve the agreement between theoretical and experimental results. Reynard and Caracas (2009) calculated reduced partition function ratios (RPFRs) of brucite and combined them with the experimental RPFRs of water vapor (Richet et al., 1977) and the experimental water–vapor fractionations (Horita and Wesolowski, 1994) to predict the H isotope fractionations between brucite and water. They considered the anharmonic corrections (e.g., Richet et al., 1977) to the RPFRs and pressure corrections (Polyakov et al., 2006) to the experimental fractionations, which yields an improved agreement with the experimental values at high temperatures, but an increased discrepancy at low temperatures. Similarly, Méheut et al. (2010) combined the calculated isotope fractionation factors of brucite-vapor with the experimental water–vapor fractionations (Horita and Wesolowski, 1994) to predict the brucite-water isotope fractionation. They also considered the pressure corrections to the experimental fractionations. Additional empirical correction obtained by fitting the difference between theoretical and experimental brucite-vapor fractionations (Eq. (6) in Méheut et al., 2010) is also applied. Their results are in good agreement with most of the experimental results and are further applied to the predictions of H isotope fractionations between water and other hydrous minerals. Colla and Casey (2019) applied the cluster method to predict the O isotope fractionations between brucite and water. Their results are different from the experimental values. By applying the corrections similar to Méheut et al. (2010), the corrected results are in good agreement with the experiments and those predicted by the semi-empirical increment method (Zheng, 1998). Overall, the corrections on the isotope fractionation factors improved the performance of the theoretical results. However, they are limited by the requirements of reliable experimental properties (e.g., the pressure dependence of RPFRs and the experimental isotope fractionation factors), which greatly hindered their application to other cases.

The unsatisfactory performance of the DFT predictions suggests that predicting the H and O isotope fractionations between brucite and water needs treatments beyond the harmonic approximation. Higher-order corrections to the Bigeleisen–Mayer equation (Bigeleisen and Mayer, 1947; Urey, 1947) have been applied to predict the D/H isotope fractionations among various systems (e.g., Richet et al., 1977; Liu et al., 2010; Zhang and Liu, 2018). However,

the treatments are too expensive for the condensed phases. Recent applications of the path-integral approach presented a new method for predicting isotope fractionations of the light elements (e.g., Markland and Berne, 2012; Pinilla et al., 2014; Dupuis et al., 2017; Turner et al., 2021). The path-integral approach treats the quantum particles as a set of ring polymer chains of P classical "beads" connected by harmonic springs (e.g., Tuckerman, 2010). The exact quantum statistics are achieved as the number of beads (i.e., P) approaches infinite. The intrinsic nature of path-integral formalism allows it to compute equilibrium isotope fractionations of light elements exactly as it takes into account the quantum and anharmonic effects (Ceriotti et al., 2016; Markland and Ceriotti, 2018). The isotope fractionation factor is related to the free energy change corresponding to an isotope substitution process. Thus, it can be computed by performing thermodynamic integration of the mean quantum kinetic energy of the interested atom as a function of the isotope mass (e.g., Vanicek and Miller, 2007; Zimmermann and Vanicek, 2009). However, the original thermodynamic estimator needs a series of independent simulations with different values of isotopic mass. For example, Pinilla et al. (2014) performed eleven independent PIMD simulations with different masses to compute the RPFR of hydrogen at a given temperature. The calculations are time-consuming. Later works proposed several more efficient estimators to accelerate the convergence and reduce the errors of the calculations (Ceriotti and Markland, 2013; Cheng and Ceriotti, 2014; Marsalek et al., 2014; Karandashev and Vaníček, 2017). The path-integral techniques have been applied to predict H, O, C, Mg, and Li isotope fractionations and clumped-isotope effects for various systems (e.g., Markland and Berne, 2012; Pinilla et al., 2014; 2015; Dupuis et al., 2017; Webb and Miller, 2014; Wang et al., 2014; 2020; Webb et al., 2017; Eldridge et al., 2019; Turner et al., 2021). However, the systems investigated are often small molecules or simple systems which have reliable force fields. This is related to the fact that first-principles path-integral molecular dynamics (FP-PIMD) simulation is too expensive, inhibiting its application to complex systems like the condensed phases.

Fortunately, recent developments in machine learning force fields (ML-FFs) allow one to generate force fields or potential energy surfaces (PESs) with first-principles accuracy for nearly any system. The pioneering work of Behler and Parrinello (2007) proposed a model called the Behler-Parrinello neural network potential (BNNP), which uses symmetry functions as input and standard neural networks as fitting functions. It provides the energies and forces with DFT accuracy and is several orders faster than DFT calculations. Later studies have also reported several models, including Gaussian approximation potential (GAP) (Bartók et al., 2010), spectral neighbor analysis potential (SNAP) (Trott et al., 2014), deep tensor neural network (DTNN) (Schütt et al., 2017), gradient-domain machine learning (GDML) method (Chmiela et al., 2017), and deep potential molecular dynamics (DPMD) scheme (Zhang et al., 2018; Wang et al., 2018). Among these models, the DPMD scheme assigns each atom a local reference frame and a local environment to respect the extensive and symmetry-invariant properties of a potential energy model. The scheme has been proved to be valid in many systems, including water (Ko et al., 2019; Zhang et al., 2021), molten alkali chlorides (Liang et al., 2021), and alloy materials (e.g., Zhang et al., 2019; Xu et al., 2020). In the field of geoscience, the DPMD scheme has also been proved to be effective in predicting diffusional isotope fractionation (Luo et al., 2021a; 2021b), viscosity, and electrical conductivity (Luo et al., 2021c) of silicate melts. These studies suggest that the DPMD scheme has the ability to generate efficient and accurate PESs for further calculations.

In this work, we combine the PIMD simulations with the trained deep potential (DP) models to predict the D/H and $^{18}O/^{16}O$ isotope

fractionations between brucite and water. To quantitatively assess the influence of quantum effects, we also calculated the isotope fractionations within the framework of harmonic approximation for comparison. The predicted fractionations with or without the quantum effects are systematically compared with previous experimental and theoretical data. Our results suggest that applying DP models in PIMD simulations could provide reasonable isotope fractionation factors for the condensed phases, which makes it a promising new tool for predicting H isotope fractionations.

2. Methods

2.1. Theories for predicting isotope fractionation factors

2.1.1. Direct estimators for isotope fractionation factors

Predicting the isotope fractionation factors using the original thermodynamic estimator needs multiple independent PIMD simulations for the discretization of the integral. To accelerate the calculations and reduce the errors, several estimators have been proposed by previous works (Ceriotti and Markland, 2013; Cheng and Ceriotti, 2014; Marsalek et al., 2014; Karandashev and Vaníček, 2017). Here, we will briefly introduce the estimator used in the present work, and the details of the estimator can be found in Cheng and Ceriotti (2014).

Assuming a system of volume V contains N particles at temperature T, the path-integral representation of its partition function has the form (e.g., Tuckerman, 2010):

$$Q(N, V, T) = \prod_{i=1}^{N} \left(\frac{m_i P}{2\pi\beta\hbar^2} \right)^{3P/2} \int \prod_{i=1}^{N} dr_i^1 dr_i^2 \cdots dr_i^P$$
$$\times \exp \left\{ -\sum_{j=1}^{P} \left[\sum_{i=1}^{N} \frac{m_i P}{2\beta\hbar^2} \left(r_i^j - r_i^{j+1} \right)^2 + \frac{\beta}{P} U(r_1^j, \cdots, r_N^j) \right] \right\}$$

(1)

where each atom in the system is represented by a ring polymer containing P classical beads connected by harmonic springs with the frequency of $P^{1/2}/\beta\hbar$. When P approaches infinite, the exact quantum statistic is achieved. β denotes the inverse temperature $1/k_B T$ and m_i is the mass of the ith atom. $U(r_1^j, \ldots, r_N^j)$ denotes the interaction potential and the coordinates of the jth bead of the ith atom are represented by r_i^j.

Considering a simple isotope exchange reaction between phase AX and X, where only one atom in AX is substituted by the heavy isotope X^*. Insert Eq. (1) into the partition function ratio of Q_{AX^*}/Q_{AX} and derive the equation:

$$\frac{Q_{AX^*}}{Q_{AX}} = \left\langle \left(\frac{m^*}{m} \right)^{3P/2} \exp \left\{ \frac{P}{2\beta\hbar^2} (m - m^*) \sum_{j=1}^{P} \left(r^j - r^{j+1} \right)^2 \right\} \right\rangle$$

(2)

where the $\langle \cdots \rangle$ represents the ensemble average over a simulation. r represents the coordinates of the substituted atom and "*" denotes the heavy isotope. The exponential function in Eq. (2) is the direct thermodynamic estimator (Z^{TD}) proposed by Cheng and Ceriotti (2014). The direct thermodynamic estimator has large fluctuations in the exponential, which is growing with the number of beads P. This makes the estimator impractical for systems with large isotope mass ratios (e.g., D/H, T/H) or in low-temperature situations (below room temperature). To reduce the statistical errors, a new estimator is obtained by applying a change of the variables into the partition function ratio:

$$r^j \leftarrow r^{(C)} + \sqrt{\frac{m^*}{m}} (r^j - r^{(C)})$$

(3)

where $r^{(C)} = \sum_j r^j / P$ represents the position of the centroid. Similarly, the direct scaled-coordinates estimator (Z^{SC}) is introduced:

$$Z^{SC} = exp \left[-\frac{\beta}{P} \sum_{j=1}^{P} U\left(r_1^{*j}, \cdots, r_N^j \right) - U\left(r_1^j, \cdots, r_N^j \right) \right]$$

(4)

The estimator requires computing the interatomic potentials, thus it is more expensive than the direct thermodynamic estimator. However, the statistical errors are much smaller at low-temperature or for large isotope mass ratio situations.

Similar formulations of estimators can also be deduced for Q_{X^*}/Q_X. Thus the fractionation factor between AX and X can be computed as:

$$\alpha_{AX-X}^{TD} = \frac{Q_{AX^*} Q_X}{Q_{AX} Q_{X^*}} = \frac{\langle Z^{TD} \rangle_{AX}}{\langle Z^{TD} \rangle_X}$$

(5)

$$\alpha_{AX-X}^{SC} = \frac{Q_{AX^*} Q_X}{Q_{AX} Q_{X^*}} = \frac{\langle Z^{SC} \rangle_{AX}}{\langle Z^{SC} \rangle_X}$$

(6)

where "$\langle \cdots \rangle$" denotes the ensemble average of the estimators over the simulations of phase AX or X. In this work, the direct scaled-coordinates estimator (Eq. (4)) is used to compute the D/H and $^{18}O/^{16}O$ isotope fractionation factors. Note that the direct scaled-coordinates estimator is the path-integral representation of the reduced partition function ratio (RPFR). In order to distinguish it from the harmonic RPFRs, we still noted it as "Z^{SC}".

2.1.2. The classical isotope fractionation theory

In this work, we also calculated the H and O isotope fractionations using the harmonic approximation. The classical equilibrium isotope fractionation theory, i.e., the Bigeleisen-Mayer equation (Bigeleisen and Mayer, 1947; Urey, 1947) is used to calculate the RPFRs of brucite and water.

According to the theory, the RPFR is closely related to the vibrational frequencies of the substance:

$$RPFR = \prod_{i}^{3N} \frac{u_i^* \exp\left(-\frac{u_i^*}{2}\right)[1 - \exp(-u_i)]}{u_i \exp\left(-\frac{u_i}{2}\right)[1 - \exp(-u_i^*)]}$$

(7)

where N is the number of atoms in the cell and the asterisks represent the heavy isotope. u_i has the form:

$$u_i = \frac{h\nu_i}{k_B T}$$

(8)

where h is the Planck's constant and ν_i is the harmonic vibrational frequency of the ith mode. k_B represents the Boltzmann's constant and T is the temperature in Kelvin. Thus, the RPFR of a substance could be calculated by computing the harmonic frequencies.

2.2. Computational details

2.2.1. Preparation of the training datasets

The training datasets are prepared by performing FPMD simulations. Ideally, the trained models can reproduce the accuracy of the training data. Wang et al. (2014) checked the isotope fractionation between water in liquid and gaseous phases by FP-PIMD simulations with several different functionals (e.g., PBE, PBE0, BLYP, and B3LYP). They found that the isotope fractionations are sensitive to the functionals. In this work, we prepare the training datasets with two functionals, i.e., the generalized gradient approximation (GGA) of PBE (Perdew et al., 1996) with D3 dispersion correction (Grimme et al., 2011) and the hybrid functional of PBE0 (Adamo and Barone, 1999). The FPMD simulations are based on the canonical ensemble (NVT) with the Nose thermostat, where the plane-wave energy cutoff is set as 600 eV and the k-point grid is $1 \times 1 \times 1$ to accelerate the running. The time step is set as 0.25 fs. The $3 \times 3 \times 2$ supercell containing 90 atoms is used for brucite, and a supercell of 32 water molecules is used for water. The

initial cell parameters are set as experimental values at room temperature. To better cover the configurational space, the volumes of initial structures are scaled by multiplying the lattice parameters with 0.975, 1.00, and 1.025 for brucite and 0.975, 1.00, 1.025, 1.050, 1.100, and 1.150 for water. The atomic positions of each structure are also perturbed. We perform the simulations at six temperatures (i.e., 273 K, 300 K, 350 K, 400 K, 500 K, and 600 K) at each volume with different initial configurations. For simulations with PBE functional, simulations are run for 80,000 steps, and the last 40,000 steps are selected as training data. For simulations with PBE0 functional, the initial structures are taken from equilibrated PBE simulations. The simulations are run for 4,000 steps for equilibration and another 8,000 steps for the selection of training data. Finally, at least 70,000 frames of the data are used for the training of each DP model, and another 6,000 frames of data are used for validation. All of the FPMD simulations are carried out with the Vienna *ab initio* simulation package (VASP) (Kresse and Furthmuller, 1996).

2.2.2. The training of DP models

The DP models are trained with the DPMD scheme (i.e., DeePMD-kit v2.0) (Wang et al., 2018), which applies deep neural networks (Goodfellow et al., 2016) to map the functions (i.e., the PES) between the atomic positions and energies/forces of the system. The total energy is evaluated by summing the atomic energies of all the atoms in the system. Each atomic energy is determined by its local environment within a cutoff radius of R_c. To preserve the translational, rotational, and permutational symmetries of the system, the original atomic coordinates are transformed into the "descriptors" (Wang et al., 2018; Zhang et al., 2018), where the "descriptors" serve as input for a deep neural network and the total energies/forces serve as output. By training the deep neural network with sufficient data, one can map the PES of a system.

For all four models trained in the present work (brucite and water with PBE and PBE0 functionals), the sizes of the embedding and fitting nets are set as {25, 50, 100} and {240, 240, 240} following those of Zhang et al. (2021). The start learning rate and decay steps are set as 0.001 and 5,000. The loss function is defined by combining the energy and force differences between the training data and DPMD predictions (in which the nuclei are classically treated with the DP models) (Wang et al., 2018; Zhang et al., 2018). The start tunable prefactors in the loss function of energy and force are set as 0.02 and 1,000 to ensure the fast convergence of the force. Each model is trained for at least 1,500,000 steps. The root-mean-square errors (RMSEs) of the energies and forces reach the accuracy levels of 1×10^{-4} eV/atom and 1×10^{-2} eV/ Å (Table 1). After the models have been trained, the models are compressed by the *deep potential compress* (Lu et al., 2022) scheme to speed up the later simulations.

2.2.3. PIMD simulations

In this work, the direct scaled-coordinates estimator (Z^{SC}) is used to calculate the isotope fractionations between brucite and water. The PIMD simulations are carried out with the i-PI package (Ceriotti et al., 2014), where the potential energies and forces are calculated with the LAMMPS package (Plimpton, 1995) by applying the DP models. To generate temperature-dependent isotope fractionation factors, we considered the brucite-water isotope fractionations at several different temperatures (i.e., 273 K, 300 K, 350 K, 400 K, 500 K, and 600 K). Firstly, the isobaric-isothermal (NPT) PIMD simulations are performed with zero pressure at each temperature for 8×10^4 steps (20 ps). The equilibrium volumes of the substances at each temperature are obtained by averaging the volumes of the last 10 ps trajectories where the average pressure is close to zero. Then the equilibrium volumes are used for the NVT simulations for $6 \times 10^5 \sim 8 \times 10^5$ steps (150 $\sim$ 200 ps) including the equilibration of 8×10^4 steps (20 ps). The time step is 0.25 fs. Each atom is modeled by 32 beads, which is sufficient to generate converged Z^{SC} values for both O and H (See Section 3.4.1). A white noise Langevin thermostat is attached to the normal mode representation (Ceriotti et al., 2010). The Z^{SC} values are computed and output every ten steps, and the final values are taken as the average of the Z^{SC} values after equilibration (>20 ps). Pinilla et al. (2014) found that the system size has a small effect on D/H isotope fractionations and a system with 32 water molecules could give a good estimation of the isotope fractionation factor. In this study, supercells containing 90 and 96 atoms are used for brucite and water. Note that the PIMD simulations are performed with two kinds of DP models which are trained on the FPMD data of PBE and PBE0 functionals. Thus we denote the simulations with the two models as "PIMD-PBE" and "PIMD-PBE0".

Previous works found that D/H isotope fractionations are sensitive to the change in pressure (Polyakov and Kharlashina, 1994; Polyakov et al., 2006; Horita et al., 1999; 2002; 2018). Systematically investigating the pressure effect on D/H isotope fractionations needs dozens of PIMD simulations, which is beyond the scope of the current study. To simply test the pressure effect, only the pressure effect at room temperature (300 K) is considered. By performing PIMD-PBE0 simulations at pressures close to 1 GPa, 2 GPa, and 3 GPa for brucite and water, the pressure-dependent isotope fractionations at 300 K could be obtained. Note that water will be in a solid phase (i.e., ice VI) when pressure is over 1 GPa at room temperature (e.g., Wagner et al., 2011; Zhang et al., 2021). By checking the radial distribution functions (RDFs) of water under high pressures (Fig. S1), we find that water may still be in the liquid phase during our simulations because the RDFs are similar to those under 0 GPa and have characteristics of short-range order and long-range disorder. Nevertheless, the isotope fractionations at high pressures presented here are the "hypothetical" values, which are used to evaluate the pressure effect on H and O isotope fractionations.

2.2.4. The computation of harmonic RPFRs

For comparison, we calculated the H and O isotope fractionations between brucite and water using the harmonic approximation. We follow the method used in our previous work (Gao and Liu, 2021) to calculate the RPFRs of brucite and water. The PBE0 functional is used to allow the harmonic RPFRs comparable to the Z^{SC} values of PIMD-PBE0 simulations. The plane wave energy cutoff is set as 600 eV. For brucite, the unit cell is firstly relaxed without constraining the atomic positions and cell parameters.

Table 1

The root-mean-square errors (RMSEs) of the energies and forces of the DP models evaluated with the training, validation, and test sets.

System	Energy (meV/atom)			Force (meV/Å)		
	Training	Validation	Test	Training	Validation	Test
Brucite (PBE)	0.13	0.17	0.11	13.48	14.95	10.78
Brucite (PBE0)	0.11	0.13	0.14	11.98	11.25	9.22
Water (PBE)	0.44	0.47	0.69	37.00	35.70	38.63
Water (PBE0)	0.48	0.57	0.46	33.53	37.21	34.80

The k-point grid is set as $9 \times 9 \times 7$. The force convergence criterion is set as 1e-3 eV/Å. After relaxation, a $4 \times 4 \times 2$ supercell is built based on the relaxed unit cell and then used for frequency calculation. The harmonic frequencies are calculated with the finite displacement method.

For water, the NPT simulation with the Langevin thermostat is performed to get the equilibrium volume at zero pressure and 300 K. The simulation cell is cubic and contains 32 water molecules. The simulation step is set as 0.25 fs and the total running time is 20 ps. The equilibrium volume is taken as the average volume of the last 10 ps, which is slightly smaller than those predicted by the PIMD simulations (10.62 ± 0.26 Å³/atom vs. 10.83 ± 0.30 Å³/atom). To include the configurational disorder of the liquid (e.g., Pinilla et al., 2015; Dupuis et al., 2015; Gao and Liu, 2021), 5 snapshots with volumes equal to the equilibrium volume are taken from the last 10 ps trajectory. The intervals of the snapshots are roughly 2 ps. Then the atomic positions of the snapshots are relaxed with the cell parameters fixed. The force convergence criterion is also set as 1e-3 eV/Å and the k-point grid is set as $1 \times 1 \times 1$. Finally, the harmonic frequencies of the 5 snapshots are calculated. Note that there are 32 oxygen and 64 hydrogen atoms in the water cell. To better include the configurational disorder, we treat all the atoms as the interested atom and totally calculated 5×32 RPFR$_O$ and 5×64 RPFR$_H$ values, the final RPFRs are taken as the average of them.

3. Results

3.1. The accuracy of the trained DP models

The energy and force root-mean-square errors (RMSEs) of the DP models evaluated with the training, validation, and test sets are summarized in Table 1. During training, the initial RMSEs of the energies and forces for training and validation sets are large, then the RMSEs decreased dramatically and finally stabilized. The average RMSEs of the energies are smaller than 1 meV/atom for all four models, and the average RMSEs of the forces are no more than 40 meV/Å. The small RMSEs imply that a good match is obtained between the DP models and FPMD calculations. The accuracy of the models is enough for the isotope fractionation calculations because the errors are much smaller than the energy change corresponding to the isotope substitution (see Section 3.3). A testing set containing 200 frames of data is used to evaluate the accuracy of the trained DP models. The energies and forces predicted by the DP models are in good agreement with those predicted by FPMD (Fig. 1, Fig. S2). The RMSEs of energy and force are comparable to those of the training and validation sets (Table 1), suggesting that the DP models are not affected by the overfitting effect.

To further assess the accuracy of the DP models, we calculated the radial distribution functions (RDFs) and the coordination numbers (CNs) of water by performing FPMD, DPMD, and PIMD simulations. Typically, the RDFs and the CNs obtained from DPMD and FPMD simulations are well overlapped with each other (Fig. S3), suggesting that the trained DP models reproduced the accuracy of the FPMD simulations in predicting the structural properties of the liquid water. The PIMD RDFs and the CNs are close to those of DPMD and FPMD simulations, but some small differences exist. For example, the PIMD O—O RDFs have slightly lower first minimums and higher second peaks, this is similar to the reported quantum and classical RDFs for water in previous works (Marsalek and Markland, 2015; Gasparotto et al., 2016; Ceriotti et al., 2016); The PIMD CNs are slightly lower than DPMD and FPMD CNs at the large distance (>2.5 ∼ 3 Å). As compared with the experiments (Soper, 2000), the theoretical RDFs roughly captured the shape of the experimental RDFs, but the theoretical RDFs

are steeper and narrower, and have higher peaks and lower minimums. This suggests that the DFT-based MD simulations predicted a more structured water environment than the experiment.

3.2. The equilibrium volumes of brucite and water at different temperatures

The DP models trained on FPMD data are used for the PIMD simulations to predict the isotope fractionations. To get fully theoretical results, the isobaric-isothermal (NPT) PIMD simulations are first conducted with zero pressure to estimate the equilibrium volumes of brucite and water at different temperatures. The results are compared with the experiments in Fig. 2. Generally, the volumes of the brucite and water increase as the temperature increases. The volume of water is much more sensitive to the temperature than brucite. At 300 K, the volumes of the water predicted by PIMD-PBE and PIMD-PBE0 are larger than the experimental values by about 8%, this is consistent with previous studies which overestimate the structural parameters of the substances by about several percent with PBE functional (e.g., Méheut et al., 2007; Gao and Liu, 2021). For brucite, the volume predicted by PIMD-PBE is larger than the experimental value by about 5% at 300 K, and the results of PIMD-PBE0 are consistent with those of experiments. To further assess the predicted volumes, we calculated the equilibrium volumes of brucite and water at 300 K with the FPMD simulations (NPT with PBE0 functional). The predicted brucite volume is in excellent agreement with those of the PIMD-PBE0 simulation (i.e., 8.22 ± 0.11 Å³/atom vs. 8.22 ± 0.09 Å³/atom). For water, the predicted equilibrium volume is smaller than the PIMD-PBE0 result by about 1.9%, (i.e., 10.62 ± 0.26 Å³/atom vs. 10.83 ± 0.30 Å³/atom), but they are in the error range of each other. The equilibrium volumes obtained from the NPT simulations are used for later NVT simulations to ensure the pressures are close to zero (Table S1).

3.3. The kinetic energies of H and O

Isotope fractionation is related to the free energy change corresponding to an isotope exchange reaction, where the change of the free energy can be estimated by integrating the quantum kinetic energy of the substituted atom as a function of the mass. Thus, checking the kinetic energies of H and O with different isotopic masses could provide important information for understanding the isotope behaviors. The quantum kinetic energy can be calculated by summing two terms, i.e., the term of classical kinetic energy independent of neighboring atoms and the term of kinetic energy associated with the quantum confinement of a particle (e.g., Vanicek and Miller, 2007; Zimmermann and Vanicek, 2009). The second term depends on the forces exerted on the particle by the surrounding atoms. If the term equals zero, then there is no isotope fractionation exists. Thus, the equilibrium isotope fractionation is a purely quantum mechanical effect (e.g., Markland and Berne, 2012; Ceriotti and Markland, 2013).

We calculated the H (K_H) and O (K_O) quantum kinetic energies in water and brucite by performing PIMD-PBE0 simulations with different isotopic masses (H vs. D and ^{16}O vs. ^{18}O). The calculated K_H and K_O as a function of temperature are presented in Fig. 3. The classical limit of kinetic energy ($3k_BT/2$) is also included for comparison. All the kinetic energies are positively correlated with the temperature. For both H and O, the quantum contribution to the kinetic energy is significant, suggesting that both H and O in brucite and water are affected by the quantum effects. As the temperature increases, the quantum effects become less important and the kinetic energies tend to converge to the classical limit. Hydrogen has larger kinetic energy than oxygen, suggesting that H atoms in brucite and water experience more significant quantum confine-
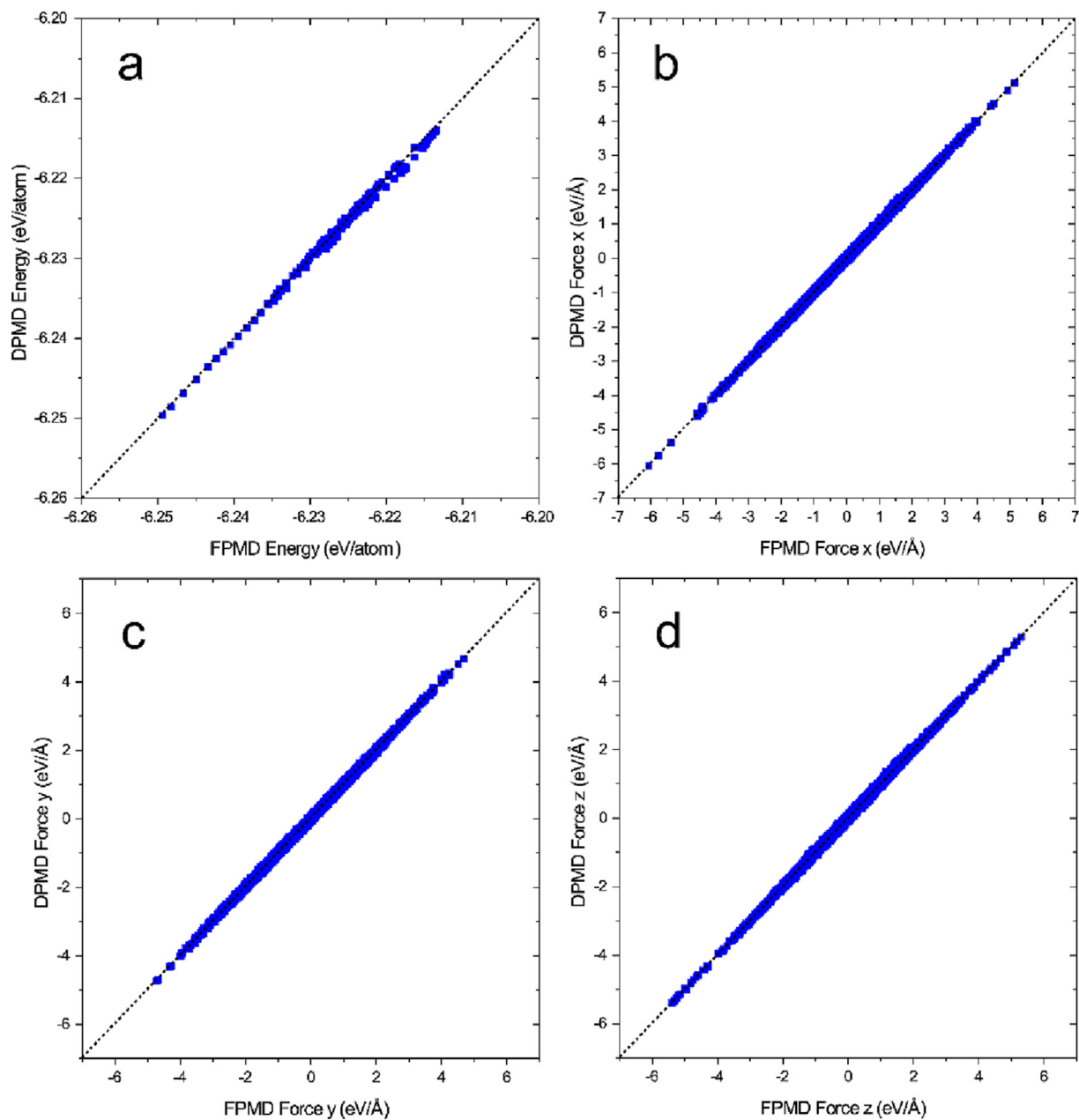
Fig. 1. Comparison of water energies and forces predicted by DPMD and FPMD (PBE0 functional). 200 frames of data are plotted in the figure. The forces of three orientations (x, y, z) acting on each atom are compared. The dotted lines represent the 1:1 correlation.

ment. Substitution of H and O in brucite and water with heavy isotopes yields smaller K_H and K_O. For hydrogen, the K_H decreases by ∼26% as changing H to D, while for oxygen the K_O decreases by ∼3% as the oxygen change from ^{16}O to ^{18}O (at 300 K). This is similar to the water kinetic energies reported by Pinilla et al., (2014). As comparing the kinetic energies of brucite and water, we find that water has larger K_H and K_O at all the temperatures studied in this work, suggesting that the quantum effects in water are slightly stronger than in brucite. This also suggests that the free energy changes of isotopic substitution reactions in water are larger than those in brucite, implying that water tends to be enriched in heavy isotopes relative to brucite.

To assess the pressure effect on the kinetic energies, we also calculated the K_H and K_O for brucite and water at 1 GPa and 300 K. The kinetic energies are compared with those at 0 GPa in Table S2. Generally, the kinetic energies at 1 GPa are larger, suggesting that pres-

sure leads to an increase in free energy change associated with isotope exchange reaction and finally yields a larger Z^{SC} value. However, an exception happens in the case of H in water. The K_H and K_D in water under 1 GPa are smaller than those under 0 GPa, which is opposite to other cases. This suggests that the free energy change associated with H-D exchange under 1 GPa is smaller than that under 0 GPa, which yields a smaller Z^{SC}. As increasing pressure yields larger Z^{SC} for H in brucite, the H isotope fractionations between water and brucite will dramatically decrease with increasing pressure.

3.4. The direct scaled-coordinates estimator (Z^{SC})

3.4.1. The convergence of the direct scaled-coordinates estimator

PIMD treats the quantum particles as a set of ring polymers of P classical beads. As P approaches infinite, the exact quantum statis-
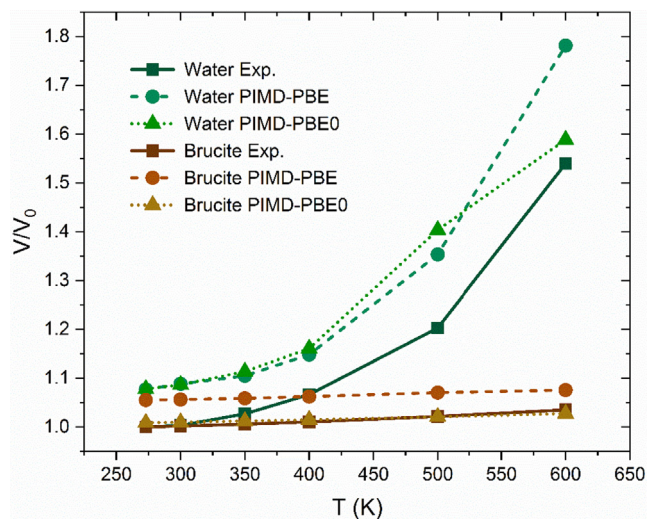
Fig. 2. The equilibrium volumes of brucite and water at different temperatures averaged from PIMD NPT trajectories. The experimental data are presented for comparison (Redfern and Wood, 1992; Wagner and Pruß, 2002). V_0 represents the experimental volumes at 273 K and V represents the volumes at elevated temperatures.
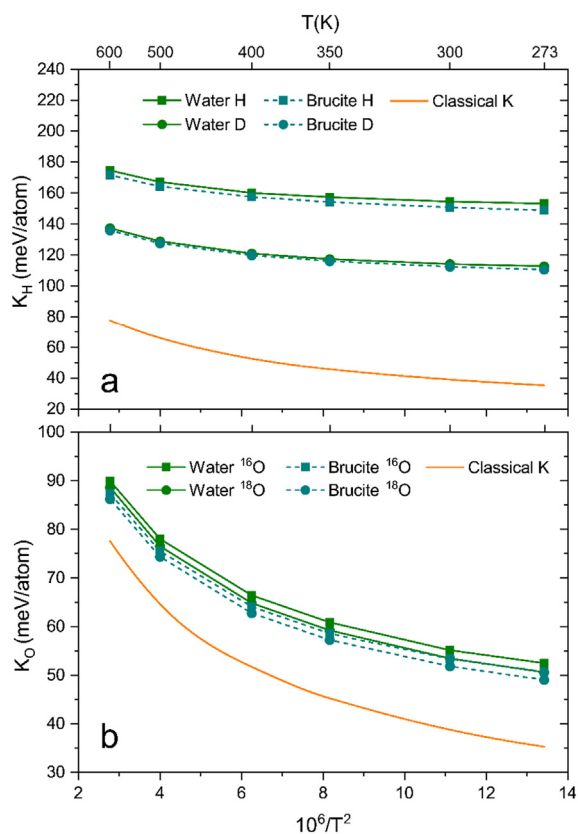

Fig. 3. Calculated H (K_H) and O (K_O) quantum kinetic energies with different isotopic masses in water and brucite as a function of temperature. The standard errors are at the order of 1×10^{-2} meV/atom, so the error bars are omitted. The classical kinetic energies ($3k_BT/2$ per atom) are also presented for comparison. (a) The kinetic energies of H; (b) The kinetic energies of O.

tics are achieved. In practice, a limited number of beads are applied to accelerate the PIMD simulations. Therefore, the convergence of the calculated properties with the number of beads P is important for the PIMD simulations. Here, the convergences of the direct

scaled-coordinates estimators and the isotope fractionation factors with the number of beads are assessed. The results suggest that the direct estimators (Z_H^{SC} and Z_O^{SC}) of brucite and water are almost converged at $P = 32$ beads (Fig. 4). As for the isotope fractionation factors, the differences between the predicted $10^3\ln(\alpha_H)$ and $10^3\ln(\alpha_O)$ with $P = 32$ and $P = 40$ are no more than 2.5‰ and 1.5‰, which suggests that 32 beads are sufficient to generate acceptable isotope fractionation factors. This is consistent with previous works which showed that 32 beads are enough to provide converged values of $10^3\ln(\alpha)$ for the liquid–vapor system (Markland and Berne, 2012; Pinilla et al., 2014). Moreover, Ceriotti and Markland (2013) suggested that the number of beads needed for convergence of the conventional PIMD simulations is proportional to $\beta\hbar\nu_{max}$, where ν_{max} is the maximum vibrational frequency of the studied system. For water and brucite ($\nu_{max} \sim 3700$ cm^{-1}) at room temperature, $P = 32$ is a safe choice to get converged isotope fractionation factors. Thus, we use 32 beads for all the PIMD simulations in the present work.

3.4.2. The predicted direct scaled-coordinates estimator

The estimated direct estimators are evaluated as the average of the $10^3\ln(Z^{SC})$ values (after equilibration) computed during PIMD simulations. The calculated $10^3\ln(Z_H^{SC})$ and $10^3\ln(Z_O^{SC})$ values and their accumulative averages of brucite and water at 300 K are presented in Fig. S4 and Fig. S5. As shown in the figures, the fluctuations of $10^3\ln(Z^{SC})$ values are large during the simulations, and the standard deviations are more than ±170‰ and ±14‰ for H and O isotopes, respectively. However, the accumulative averages of brucite and water are stabilized after the first 20 ps, and their values are clearly different. The estimated values of $10^3\ln(Z_H^{SC})$ (PIMD-PBE0) for brucite and water are 2466.1 ± 0.73‰ and 2527.0 ± 0.61‰ at 300 K, and the $10^3\ln(Z_O^{SC})$ values are 63.0 ± 0.04‰
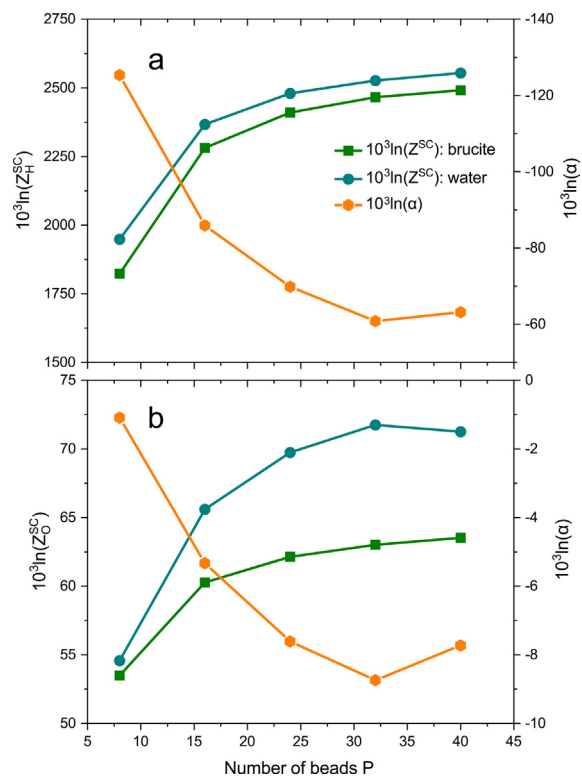

Fig. 4. The variations of $10^3\ln(Z^{SC})$ and $10^3\ln(\alpha)$ (‰) with the number of beads (PIMD-PBE0 at 300 K). The squares and circles represent the $10^3\ln(Z^{SC})$ values of brucite and water, and the hexagons denote the corresponding isotope fractionations. (a) H isotope; (b) O isotope.

and 71.7 ± 0.05‰ (Fig. S4 and Fig. S5). The standard errors are smaller than 1‰, which ensures the accuracy of the estimated direct estimators.

The estimated direct estimators and equilibrium isotope fractionation factors at temperatures between 273 K and 600 K are presented in Table 2 and Fig. 5. Generally, the $10^3\ln(Z^{SC})$ values decrease as the temperature increases. The values estimated by PIMD-PBE0 and PIMD-PBE are different, this is related to the fact that the DP models are trained on FPMD data of different functionals. For H isotopes, both the results of PIMD-PBE0 and PIMD-PBE suggest that water is enriched in D relative to brucite, this is consistent with previous experimental and theoretical results (Satake and Matsuo, 1984; Xu and Zheng, 1999; Saccocia et al., 1998; Horita et al., 1999; 2002; 2018; Reynard and Caracas, 2009; Méheut et al., 2010). For oxygen isotope, our results suggest that water is also enriched in heavy O isotope relative to brucite. By comparing the predicted $10^3\ln(Z^{SC})$ values, the isotope fractionation factors between brucite and water can be estimated (Table 2).

The pressure effects on H and O isotope fractionations at 300 K are investigated by performing PIMD simulations at pressures close to 1 GPa, 2 GPa, and 3 GPa. The pressure dependences of $10^3\ln(Z^{SC})$ values are presented in Fig. 6 and Table S3. For H, the calculated $10^3\ln(Z^{SC}_H)$ values of brucite are gradually increasing with the increase of pressure, but the $10^3\ln(Z^{SC}_H)$ values of water are decreasing as the pressure increase, indicating that the D/H isotope fractionation between water and brucite decreases with the increase of pressure. This is consistent with the demonstrations based on the kinetic energies in Section 3.3 and those reported by previous works (Polyakov and Kharlashina, 1994; Horita et al. 2002). The $10^3\ln(Z^{SC}_H)$ values of brucite and water are nearly identical around the pressure of 3 GPa, as the pressure increases, the D/H isotope fractionation between brucite and water will be inversed. For O, both the $10^3\ln(Z^{SC}_O)$ values of brucite and water are increasing with the increase of pressure. Thus the change of $^{18}O/^{16}O$ isotope fractionation with pressure is relatively small as

Table 2
The predicted $10^3\ln(Z^{SC})$ (‰) of brucite and water at different temperatures (PIMD-PBE0 and PIMD-PBE). The H and O isotope fractionation factors (‰) between brucite and water at different temperatures are also presented. Note that the pressures of the PIMD simulations are not strictly zero (Table S1). The values in the brackets are the $10^3\ln(Z^{SC})_{Corrected}$ values at zero pressure and 300 K (see Table S3 for details).

| T (K)	Brucite		Water		Brucite vs. Water	
	$10^3\ln(Z^{SC}_H)$	$10^3\ln(Z^{SC}_O)$	$10^3\ln(Z^{SC}_H)$	$10^3\ln(Z^{SC}_O)$	$10^3\ln(\alpha_H)$	$10^3\ln(\alpha_O)$
PIMD-PBE0						
273	2757.0	73.0	2835.4	81.2	−78.3	−8.2
300	2466.1 (2466.3)	63.0(63.0)	2527.0(2529.9)	71.8(71.7)	−60.9(−63.7)	−8.7(−8.6)
350	2045.3	49.6	2087.0	57.4	−41.7	−7.9
400	1730.8	40.2	1761.7	47.6	−30.9	−7.4
500	1295.0	28.2	1322.2	34.6	−27.2	−6.4
600	1009.6	21.1	1036.1	26.8	−26.6	−5.7
PIMD-PBE						
273	2618.6	67.4	2677.7	78.2	−59.1	−10.8
300	2339.3	58.3	2379.8	69.4	−40.5	−11.1
350	1936.1	45.8	1959.1	55.6	−23.0	−9.8
400	1635.6	37.1	1648.5	45.7	−12.9	−8.6
500	1220.3	26.1	1235.5	32.9	−15.2	−6.8
600	948.5	19.5	968.7	25.1	−20.2	−5.6
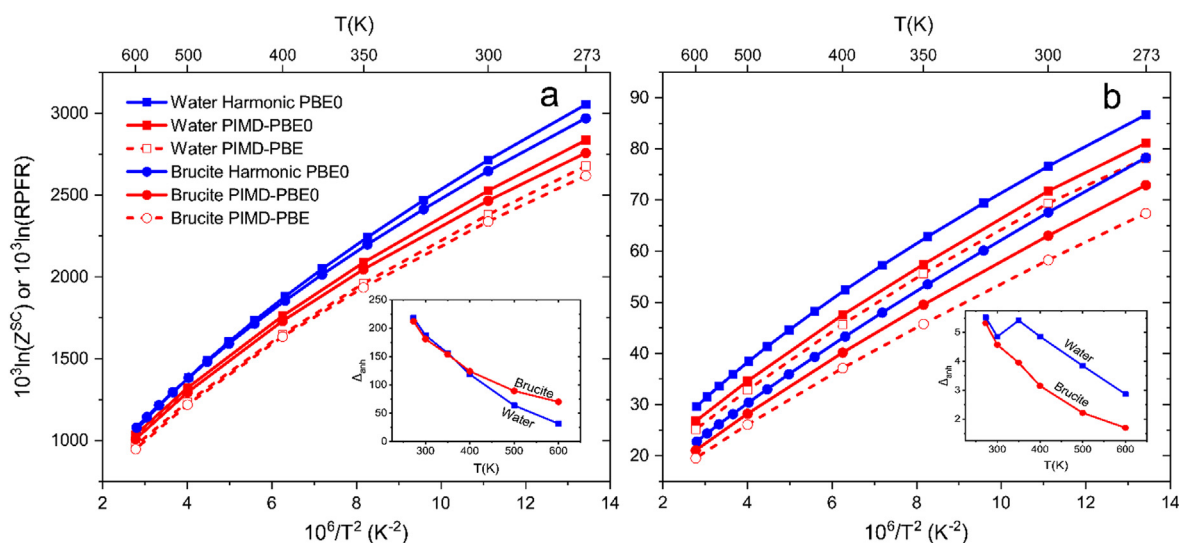
Fig. 5. The temperature dependence of $10^3\ln(Z^{SC})$ (‰) of brucite and water (PIMD-PBE0 and PIMD-PBE). The harmonic RPFRs in ‰ are presented for comparison. The insets represent the differences (Δ_{anh} in ‰) between harmonic RPFRs and the Z^{SC} at different temperatures. (a) H isotope; (b) O isotope.
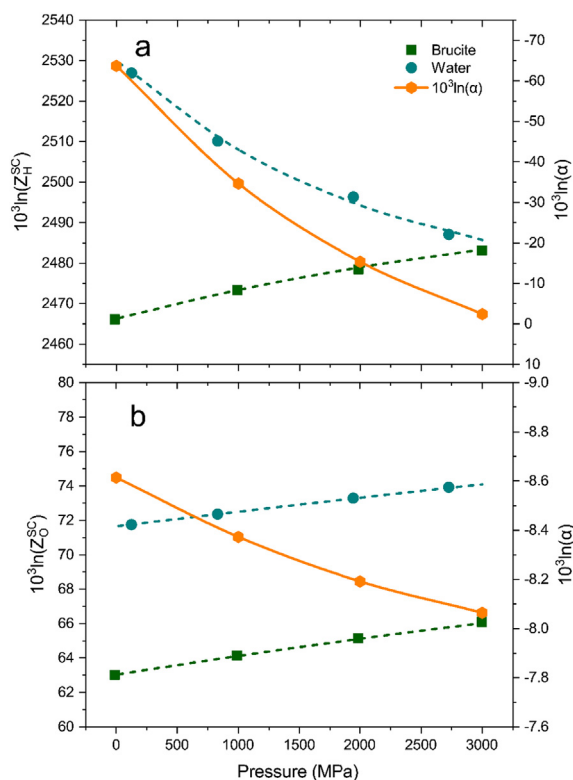
Fig. 6. The pressure dependence of $10^3\ln(Z^{SC})$ (‰) of brucite (squares) and water (circles) at 300 K (0–3 GPa, PIMD-PBE0). The dashed lines represent the fitting curves of the $10^3\ln(Z^{SC})$ values (Table S3). The isotope fractionations (hexagons) at different pressures are also presented. (a) H isotope; (b) O isotope.

pressures and the expected pressures. As for the O isotope, the corresponding corrections are small (<0.2‰), suggesting its fractionation is less sensitive to the pressure change relative to the H isotope. For brucite, the PIMD pressures are close to the expected pressures, so the corrections for both H and O isotopes are small (<0.5‰).

3.5. The harmonic RPFRs

To assess the contribution of the quantum effects and anharmonicity, we calculated the harmonic RPFRs for brucite and water. The structural and vibrational parameters of brucite are compared with previous measurements (Chakoumakos et al., 1997; Dawson et al., 1973) and calculations (Méheut et al., 2010; Reynard and Caracas, 2009) in Table S4. The predicted RPFRs are shown in Table 3 and Fig. 5. Generally, water has larger RPFRs than brucite, indicating that the heavy isotopes tend to be enriched in water rather than brucite. As compared with the Z^{SC} values of PIMD-PBE0, RPFRs are significantly larger than Z^{SC}, which suggests that the quantum effects have a large influence on the isotope behaviors in brucite and water. As the temperature increases, the RPFR values tend to converge to the Z^{SC} values. This is similar to the temperature dependence of the quantum kinetic energies (Fig. 3), suggesting that the quantum effects are less relevant at high temperatures. The H and O isotope fractionations calculated with harmonic RPFRs are also listed in Table 3. The errors of the isotope fractionations are taken as the standard deviations of water RPFRs.

4. Discussions

4.1. Comparing the estimated pressure effect with previous studies

The pressure effect on H isotope fractionation between brucite and water has been studied by previous theoretical and experimental works (Polyakov and Kharlashina, 1994; Polyakov et al., 2006; Horita et al., 1999; 2002; 2010; 2018), the experimental works are mainly focused on the situations of 200–600 °C and 0–800 MPa. The pressure effect is usually quantified by the ratio of RPFRs of the substance at a given pressure (p_g) and a reference pressure (p_{ref}), namely $10^3\ln(\frac{RPFR_{p_g}}{RPFR_{p_{ref}}})$. In this work, we only calculated the $10^3\ln(Z^{SC})$ values at 300 K in the pressure range of 0–3 GPa (Table S3, Fig. 6). We find that the estimated $10^3\ln(Z^{SC})$ values all increase with the increase of pressure, except for the $10^3\ln(Z_H^{SC})$ values of water, which are in the opposite direction. This is related

compared to the D/H isotope fractionation. Note that the pressures in Fig. 6 are taken as the average pressures of the PIMD simulations, their values are not strictly equal to the expected pressures (i.e., 0 GPa, 1 GPa, 2 GPa, and 3 GPa), especially for water (Table S3). We can easily correct the $10^3\ln(Z^{SC})$ values to those at the expected pressures by fitting the $10^3\ln(Z^{SC})$–pressure relations (Table S3). At zero pressure, the $10^3\ln(Z_H^{SC})_{Corrected}$ value of water (~2529.9‰) is larger than the calculated value (~2527.0‰) by about 3‰ (Table 2). At other pressures, the $10^3\ln(Z_H^{SC})_{Corrected}$ values deviate from the calculated values by about 2‰ (Table S3). The corrections are related to the differences between the PIMD

Table 3

The harmonic RPFRs (‰) of brucite and water at different temperatures. The H and O isotope fractionations (‰) are also presented. The RPFRs are calculated with PBE0 functional. For water, the values of $RPFR_H$ and $RPFR_O$ are taken as the average of 5×64 and 5×32 RPFR values, respectively. The errors of the isotope fractionations are taken as the standard deviations of the RPFRs of water.

T (K)	Brucite		Water		Brucite vs. Water	
	$10^3\ln(RPFR_H)$	$10^3\ln(RPFR_O)$	$10^3\ln(RPFR_H)$	$10^3\ln(RPFR_O)$	$10^3\ln(\alpha_H)$	$10^3\ln(\alpha_O)$
273	2969.3	78.3	3053.8	86.7	−84.5 ± 17.0	−8.4 ± 2.5
300	2646.9	67.6	2714.4	76.6	−67.5 ± 14.9	−9.0 ± 2.1
323	2414.0	60.2	2469.2	69.4	−55.2 ± 13.9	−9.3 ± 1.8
348	2199.2	53.5	2242.9	62.8	−43.7 ± 13.3	−9.3 ± 1.5
373	2014.8	48.0	2048.7	57.2	−33.9 ± 13.1	−9.3 ± 1.3
398	1854.9	43.3	1880.3	52.4	−25.4 ± 13.2	−9.1 ± 1.1
423	1714.9	39.4	1733.1	48.2	−18.1 ± 13.4	−8.9 ± 1.0
448	1591.6	36.0	1603.4	44.6	−11.8 ± 13.6	−8.6 ± 0.9
473	1482.1	33.0	1488.4	41.3	−6.3 ± 13.8	−8.3 ± 0.8
498	1384.2	30.4	1385.8	38.5	−1.6 ± 13.9	−8.0 ± 0.7
523	1296.4	28.2	1293.8	35.9	2.6 ± 14.1	−7.7 ± 0.6
548	1217.0	26.2	1210.9	33.6	6.1 ± 14.1	−7.4 ± 0.6
573	1145.1	24.4	1135.9	31.5	9.2 ± 14.2	−7.1 ± 0.5
598	1079.6	22.8	1067.7	29.6	11.9 ± 14.2	−6.9 ± 0.5
623	1019.7	21.3	1005.6	27.9	14.2 ± 14.1	−6.6 ± 0.4

to the fact that the mole volume (V) of the H_2O in the liquid phase is smaller than that of D_2O (Kell, 1977). Thus the differential of the RPFR with respect to the pressure is smaller than 0, i.e., $\left(\frac{\partial \ln(RPFR)}{\partial p}\right)_T = -\frac{\Delta V}{nRT} < 0$ ($\Delta V = V^* - V$) (Clayton et al., 1975; Polyakov, 1998), while most of the other compounds have $\left(\frac{\partial \ln(RPFR)}{\partial p}\right)_T = -\frac{\Delta V}{nRT} > 0$. Similar results are also found by previous works (Polyakov and Kharlashina, 1994; Horita et al. 2002).

Horita et al. (2002) theoretically predicted the pressure effect on RPFRs of brucite, they found that the $10^3\ln(RPFR)$ of brucite increased by 12.58‰ from 0 MPa to 800 MPa with an error of ±5~10% (i.e., $10^3\ln\left(\frac{RPFR_{p=800}}{RPFR_{p=0}}\right) = 12.58‰$ at 300 K). Zhu et al. (2019) considered the anharmonic contribution to the pressure effect on brucite RPFRs, their results are slightly smaller than those of Horita et al. (2002) at 300 K ($10^3\ln\left(\frac{RPFR_{p=800}}{RPFR_{p=0}}\right) = 12.17‰$). Reynard and Caracas (2009) predicted the pressure effect on RPFRs of brucite based on the quasi-harmonic approximation, which yields $10^3\ln\left(\frac{RPFR_{p=800}}{RPFR_{p=0}}\right) = 10.39‰$ at 300 K. In this work, the estimated pressure effect of brucite is $10^3\ln\left(\frac{Z^{SC}_{H,p=800}}{Z^{SC}_{H,p=0}}\right) = 5.8 \pm 4.5‰$, which is in the same direction of the previous results, but the magnitude of pressure effect is smaller. For water, Polyakov et al. (2006) developed a theoretical approach based on equations of state to estimate the RPFRs of water at elevated temperatures (up to 527 °C) and pressures (0–100 MPa). They found that the $10^3\ln\left(\frac{RPFR_{p=100}}{RPFR_{p=0}}\right)$ value of water is about −0.9‰ at 30 °C and −1.4‰ at 10 °C (see Fig. 6 in Polyakov et al., 2006). In this work, the estimated $10^3\ln\left(\frac{Z^{SC}_{H,p=100}}{Z^{SC}_{H,p=0}}\right)$ is −2.7 ± 12.6‰ for water at 300 K. Despite the large standard errors, the result is close to that of Polyakov et al. (2006). The pressure dependence of the D/H isotope fractionation factor is also presented in Fig. 6. The fractionation factors increase from −63.7‰ at 0 GPa to −2.4‰ at 3 GPa. As the pressure continuously increases, the D/H isotope fractionation between brucite and water has the trend to be inversed. The trend is consistent with that of Horita et al. (2010), which suggested that the D/H isotope fractionations between brucite and water under high pressures will be different from those of near-surface environments.

Previous experimental works found no measurable O isotope pressure effect in mineral–water systems at pressures up to 2.2 GPa (400–700 °C) (e.g., Clayton et al., 1975; Matsuhisa et al., 1979; Matthews et al., 1983a; 1983b). However, Polyakov and Kharlashina (1994) and Polyakov (1998) theoretically found a measurable O isotope pressure effect on minerals. In this work, the predicted $10^3\ln(Z^{SC}_O)$ values of brucite and water are increasing with the increase of pressure (Fig. 6, Table S3). The estimated $10^3\ln\left(\frac{Z^{SC}_{O,p=3000}}{Z^{SC}_{O,p=0}}\right)$ values of brucite and water are 2.99‰ and 2.44‰ at 300 K, which are much less than those of the H isotope, suggesting that the O isotope fractionation is less sensitive to the pressure change. Because the estimated pressure effect on the O isotope of brucite and water are comparable, the overall pressure effect on the isotope fractionation factor is small (increased from –8.62‰ at 0 GPa to –8.07‰ at 3 GPa). At high temperatures, the pressure effect on the O isotope fractionation factors may be much smaller, this might explain why previous experimental work found no discernible pressure effects on $^{18}O/^{16}O$ isotope fractionations.

4.2. The influence of including the quantum effects

In this work, we calculated the H and O isotope fractionations between brucite and water by PIMD simulations and harmonic cal-

culations. The PBE0 functional is used in both approaches to ensure that the calculated Z^{SC} and RPFR values are comparable. As shown in Fig. 5, the inclusion of the anharmonic effects leads to decreases in the RPFRs for both brucite and water, suggesting that both H and O in the two phases are affected by the anharmonicity. This is different from those found by Dupuis et al. (2017), which observed significant anharmonicity in the aqueous solution of Li⁺, but for Li⁺ in Li_2O solid, the contribution of anharmonicity to the RPFRs is negligible.

The influence of anharmonic effects can be evaluated by $\Delta_{anh} = 10^3\ln(RPFR) - 10^3\ln(Z^{SC})$. The temperature dependence of Δ_{anh} is shown in the insets of Fig. 5. For the H isotope, the Δ_{anh} value for water is ~218‰ at 273 K and dramatically decreases to ~32‰ at 600 K. Brucite has Δ_{anh} values close to those of water at low temperatures (<400 K), the anharmonicity could be largely canceled when calculating the isotope fractionations (Méheut et al., 2010; Webb and Miller, 2014). However, the anharmonicity is only partially canceled at high temperatures (>400 K), because the Δ_{anh} values for brucite and water are significantly different. For the O isotope, the anharmonic contribution to RPFR is also significant, e.g., Δ_{anh} has a value of 5.5‰ for water at 273 K and a value of 2.9‰ at 600 K. Similar to the H isotope, the cancellation of anharmonicity exists at low temperatures (<300 K), but at temperatures larger than 300 K, the anharmonicity is only partially canceled. Note that the harmonic calculations in this work used the volumes of low temperatures and neglected the temperature dependence of the volumes (Fig. 2). The $RPFR_H$ of water may be underestimated at high temperatures, whereas the RPFRs of brucite and the $RPFR_O$ of water may be overestimated because of the pressure effect (Fig. 6). Thus the Δ_{anh} values of water at high temperatures are different from those of brucite for both H and O isotopes. Considering this, it is possible that the anharmonic effects on brucite and water are comparable at all the temperatures studied in this work and can be mostly canceled when calculating the isotope fractionation factors (Méheut et al., 2010). The prerequisite is including the temperature dependence of the volumes when calculating the RPFRs, especially for systems with their volumes sensitive to the temperature (e.g., liquid water). Systematic investigation of the cancellation of anharmonicity in the brucite-water system needs a large number of calculations, which is beyond the scope of the current study. Nevertheless, the results suggest that the anharmonic effects have a large influence on the RPFRs of both brucite and water. The similarity of the anharmonic effect in the two phases leads to the cancellations of the Z^{SC} values at low temperatures and yields isotope fractionations close to those predicted by harmonic calculations.

To further assess the influence of quantum effects, we calculated the partial vibrational density of states (PVDOS) of the H atoms in brucite and water at 300 K using the trajectories of DPMD and PIMD simulations. The PVDOS curves are calculated using *nMoldyn* (version 3.0.11) (Róg et al., 2003). For water, the PVDOS has three bands (Fig. 7a), which represent the intermolecular vibrations, bending, and stretching vibrations of H_2O molecules in liquid water. The positions of the peaks are close to those of previous MD simulations for water (Praprotnik et al., 2004). For brucite, the PVDOS also has three bands (Fig. 7b). The band of stretching modes is located in the higher frequency region as compared to the PVDOS of water, suggesting that the O—H covalent bonds in brucite are stronger than those in water. The band of bending vibrations remarkably shifts to the lower frequencies because the O atom in brucite forms four covalent bonds with H and Mg, which weakens the bending vibrations. The libration peak of brucite is also located in the lower frequency region, suggesting that the librations are suppressed in brucite.

As shown in Fig. 7, including the quantum effects for water shifts the bands of bending and stretching vibrations to the lower
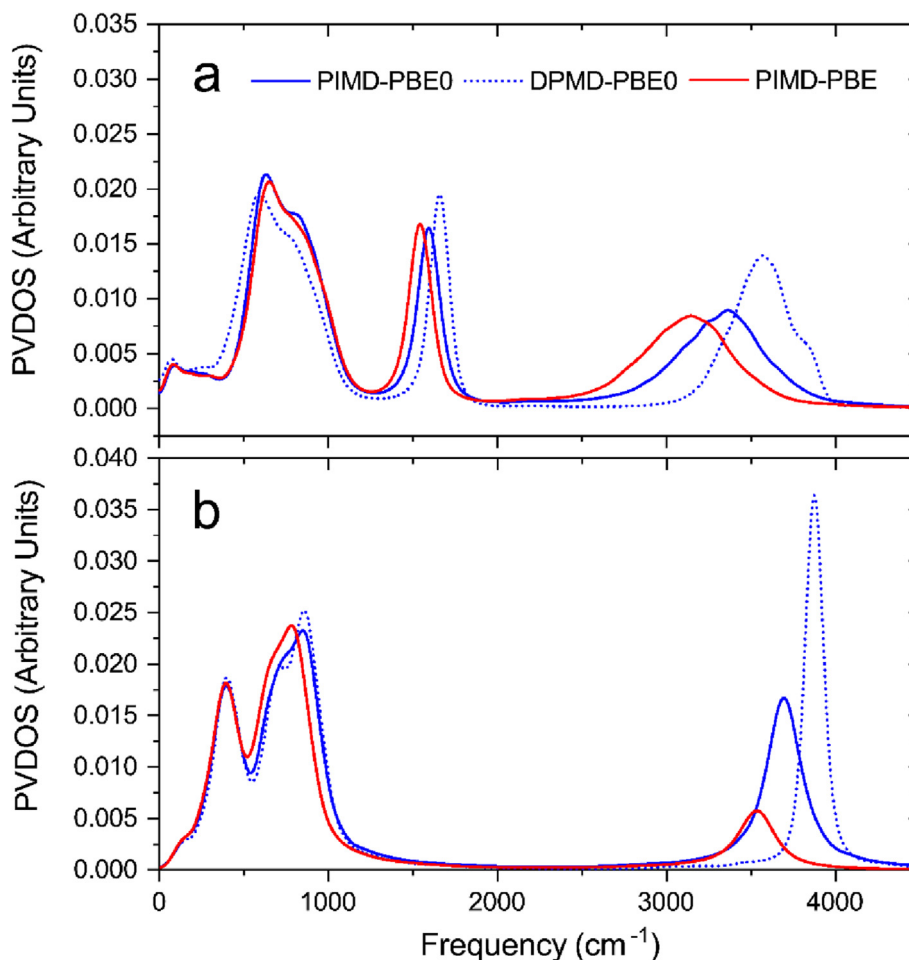
Fig. 7. The PVDOS of the H atoms in water and brucite at 300 K. The curves generated from PIMD-PBE0, DPMD-PBE0, and PIMD-PBE trajectories are presented for comparison. (a) Water; (b) Brucite.

frequencies and become broader and shorter, while the band of intermolecular vibrations shifts to the higher frequencies and becomes higher. This suggests that the quantum effects weaken the O—H covalent bond in water molecules and strengthen the hydrogen bonding among water molecules (e.g., Wang et al., 2014; Ceriotti et al., 2016). Similarly, including the quantum effects for brucite shifts the band of stretching vibrations to lower frequencies and weakens the O—H covalent bonds. However, the PIMD curves are nearly overlapped with those of DPMD in the low-frequency region (<1500 cm^{-1}), only the heights of peaks are slightly lower. From these results, it is clear that including the quantum effect will decrease the O—H stretching and bending frequencies of relevance to the isotope fractionations. This could explain why the Z^{SC} values are smaller than the harmonic RPFRs (Fig. 5).

4.3. The equilibrium D/H isotope fractionation factors between brucite and water

The D/H isotope fractionation factors predicted by PIMD simulations and harmonic calculations are compared with those of previous works in Fig. 8. Generally, the $10^3\ln(\alpha)$ of PIMD-PBE and PIMD-PBE0 are different, with the results of PIMD-PBE0 being closer to the experiments. This is consistent with previous FP-PIMD work (Wang et al., 2014), which found that including the exact exchange in functionals leads to a much-improved agreement for isotope fractionation factors. As demonstrated by Wang et al.

(2014), the PBE simulation predicts a larger proton excursion probability than PBE0 simulations. The increased proton sharing in PBE simulation weakens the O—H covalent bond in water and yields a more negative water–vapor isotope fractionation. In this work, we calculate the PVDOS of the H atoms in brucite and water by PIMD-PBE and PIMD-PBE0 simulations (Fig. 7). The PIMD-PBE simulations shift the bands of stretching and bending vibrations to lower frequencies as compared to the PIMD-PBE0 simulations. This suggests that the PIMD-PBE simulations predict more proton sharing in both brucite and water, which yields smaller Z^{SC} values relative to those of PIMD-PBE0 simulations (Table 2; Fig. 5). Thus the PIMD-PBE simulations finally predict smaller absolute isotope fractionations.

The isotope fractionations predicted by PIMD-PBE0 simulations are consistent with the harmonic calculations at temperatures smaller than 400 K (Fig. 8). The consistency is the result of the cancellation effect, because the Δ_{anh} values of brucite and water are very close (Fig. 5a inset), which leads to the cancellation of the anharmonic effect when calculating the isotope fractionation factors. At higher temperatures, the isotope fractionations of PIMD-PBE0 are more negative than harmonic results, this is because the Δ_{anh} values of brucite and water are different and the anharmonic effects are only partially canceled. As demonstrated in Section 4.2, the anharmonic effects on brucite and water may be comparable at all the temperatures studied in this work. If the temperature dependence of the volumes is considered for brucite and water, it is likely that the harmonic isotope fractionations at high
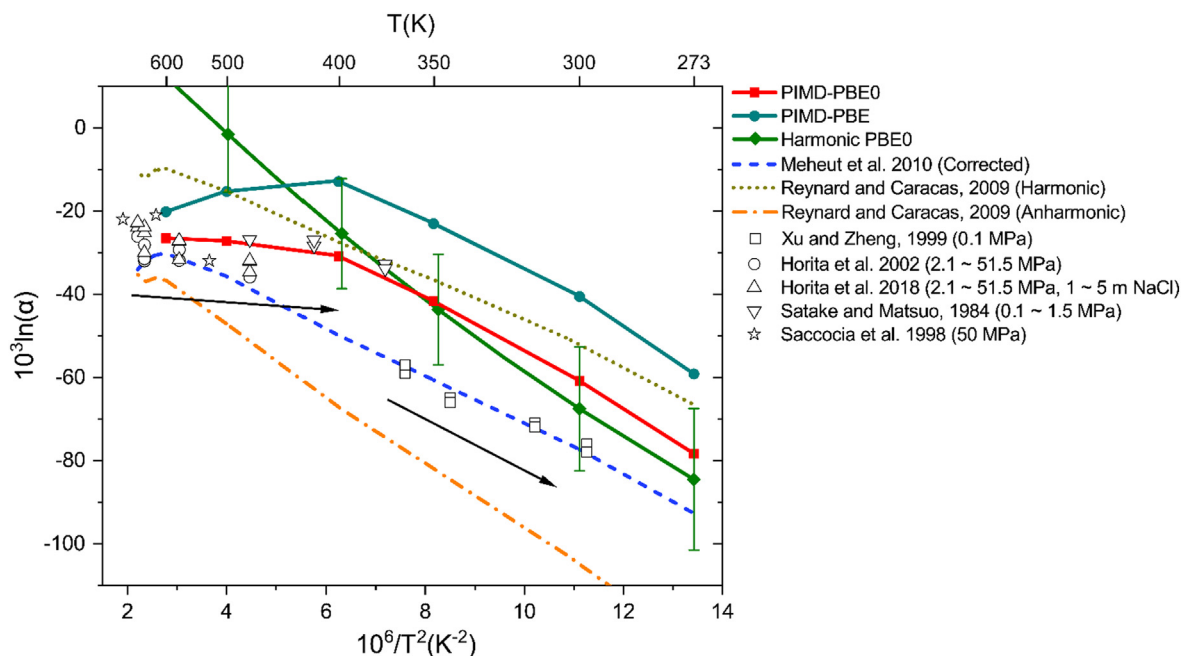
Fig. 8. The PIMD and harmonic D/H isotope fractionation factors (‰) between brucite and water. Previous experimental (Horita et al., 2002, 2018; Saccocia et al., 1998; Satake and Matsuo, 1984; Xu and Zheng, 1999) and theoretical (Reynard and Caracas, 2009; Méheut et al., 2010) results are presented for comparison. For experiments, only the low-pressure ($\leq$51.5 MPa) data are presented. The black arrows denote the two-part $10^3\ln(\alpha)$–temperature relations for the D/H isotope fractionation.

temperatures are also close to the PIMD results due to the cancellation effect. Nevertheless, by comparing the results of PIMD and harmonic calculations, we find that the accuracy of the harmonic calculations largely depends on the similarity in anharmonic contributions to the RPFRs (Δ_{anh}) of the materials (Dupuis et al., 2017).

The D/H isotope fractionations between brucite and water have been investigated by several experimental works (Satake and Matsuo, 1984; Saccocia et al., 1998; Xu and Zheng, 1999; Horita et al., 1999; 2002; 2018). Based on the experimental data, the temperature dependence of D/H isotope fractionations can be divided into two parts (Fig. 8): (1) At low temperatures (<100 °C), the $10^3\ln(\alpha)$ is significantly increasing as the temperature increases; (2) At high temperatures (>100 °C), the temperature dependence of $10^3\ln(\alpha)$ is weaker than those at low temperatures. In this work, the harmonic isotope fractionations are close to the experiments (Xu and Zheng, 1999) at room temperature due to the cancellation of the anharmonic effects. At high temperatures (>400 K), the anharmonic effects are only partially canceled, and the harmonic $10^3\ln(\alpha)$ are significantly larger. For PIMD-PBE0 simulations, the results successfully captured the two-part temperature dependence of the isotope fractionations and are in good agreement with the experiments conducted at high temperatures (>100 °C) (Satake and Matsuo, 1984; Saccocia et al., 1998; Horita et al., 2002; 2018). However, at low temperatures, the $10^3\ln(\alpha)$ values are larger than those of the experiment (Xu and Zheng, 1999) by more than 10‰ (−63.7‰ vs. −77‰ at 300 K). The discrepancy may be related to the errors involved in the PIMD simulations.

In this work, the non-zero pressures of the PIMD simulations may introduce errors to the final isotope fractionations (Table S1). For example, the predicted $10^3\ln(\alpha_H)$ between brucite and water at 300 K is −60.9‰ (Table 2), and the corresponding average pressures are −12.74 MPa and 125.25 MPa for the simulations of brucite and water (Table S1). After correcting the pressure effect, the predicted $10^3\ln(\alpha_H)$ decreased to −63.7‰ (Table 2), indicating that the non-zero pressures of the PIMD simulations have a *permil* level effect on the $10^3\ln(\alpha)$ values. However, such an effect is not enough to explain the discrepancy between this work and Xu

and Zheng (1999). Moreover, most of the absolute average pressures of the PIMD simulations are smaller than 65 MPa (except for water at 273 K and 300 K) (Table S1), which further indicates that the discrepancy between theoretical and experimental works is not caused by the non-zero pressures of the PIMD simulations.

Another main source of error in our calculations may arise from the application of the Born-Oppenheimer (BO) approximation, which allows the nuclear and electronic motions to be separated. In this study, the training data are generated within the framework of BO approximation. The application of the DP models assumes that the potential energies of all the isotopologues are identical, which is valid for most situations. However, for substances that contain light elements (e.g., H), neglecting the difference between the potential energies of the isotopologues may lead to large errors in the predicted isotope fractionation factors (Zhang and Liu, 2018; Turner et al., 2021). Here, the diagonal Born-Oppenheimer corrections (DBOCs) (Born and Huang, 1956) are calculated for brucite and water clusters (Table S5; Table S6). As demonstrated in the Supplementary materials, considering the DBOCs has little impact on improving the agreement between theoretical and experimental works. This suggests that the discrepancy in isotope fractionations at low temperatures is not caused by the application of the BO approximation.

Previous PIMD works (Markland and Berne, 2012; Wang et al., 2014) found that the overall water–vapor H isotope fractionation is the consequence of the partial cancellation of the decomposed isotope fractionations in the three directions of each water molecule, i.e., the direction along the O—H covalent bond vector and the other two directions perpendicular to the O—H covalent bond. The H isotope fractionation in the O—H direction is negative, while the fractionations in the other two directions are positive. In the case of brucite-water, the overall $10^3\ln(\alpha_H)$ can also be regarded as the results of the partial cancellation of the decomposed isotope fractionations in the different directions, i.e., the direction along the O—H covalent bond vector and the other direction perpendicular to the O—H covalent bond. The fractionation in the O—H direction is closely related to the stretching vibrations of O—H bonds in

brucite and water, while the fractionation in the other direction is related to the librations and bending vibrations. By checking the PVDOS of H atoms in the two phases (Fig. 7), we find that brucite possesses stronger O—H covalent bonds but weaker hydrogen bonds relative to the water, suggesting that the O—H direction contribution to the brucite-water isotope fractionation is positive, but the contribution of the perpendicular direction is negative. Wang et al. (2014) reported a large variation range of water–vapor $10^3\ln(\alpha_H)$ ($-17‰ \sim 102‰$ at 300 K) with different functionals (PBE, BLYP, PBE0, and B3LYP). The accuracy of the $10^3\ln(\alpha_H)$ values depends on the cancellation percentage of the fractionations in different directions, i.e., the accuracy of the DFT functionals in predicting the proton delocalization. Their PBE functional overestimated the proton excursion while other functionals predicted relatively accurate proton positions. Their result of PBE0 simulation differs from the experimental value by about 17‰, which is similar to the predicted fractionations in this work. From these results, it is likely that the discrepancy between this work and Xu and Zheng (1999) at low temperatures is related to the approximations in the DFT functional. Maybe more accurate functionals or higher-level theoretical methods are needed for the PIMD simulations, but they are currently too expensive for the FPMD simulations of the condensed phases. It is also possible that the discrepancy is related to the quantum effects, as they are more relevant at low temperatures.

4.4. The equilibrium $^{18}O/^{16}O$ isotope fractionation factors between brucite and water

The predicted $^{18}O/^{16}O$ isotope fractionations between brucite and water are compared with previous measurements and estimations in Fig. 9. Similar to the H isotope fractionations, the O isotope fractionations predicted by PIMD-PBE simulations are different from those of PIMD-PBE0 simulations. The harmonic isotope fractionations are close to the PIMD-PBE0 results at low temperatures (<300 K) due to the cancellation of the anharmonic effects. At higher temperatures, the anharmonic effects are only partially canceled, so the results of the two approaches are different. As compare the predicted isotope fractionations with the experiments (Saccocia et al., 1998; 2015; Xu and Zheng, 1999), the predicted PIMD-PBE0 $10^3\ln(\alpha_O)$ values are different from those of experi-
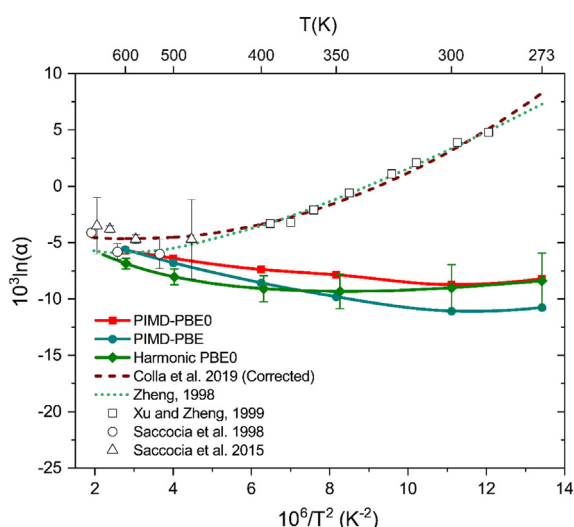
ments at low temperatures, but in acceptable agreement with those at high temperatures (>200 °C) (Fig. 9). This is similar to the H isotope fractionations. At 300 K, the difference between the predicted $10^3\ln(\alpha_O)$ values of the present work and the previous experiment (Xu and Zheng, 1999) is more than 10‰. The non-zero pressures of our PIMD simulations have little effect ($\sim$0.1‰) on the final $10^3\ln(\alpha_O)$ values (Table 2). As for DBOC, the correction factors for $^{18}O/^{16}O$ isotope fractionations are no more than 0.3‰ at the temperature range of 273 K to 600 K (Table S6), which could not explain the large discrepancy. It is possible that the discrepancy is also related to approximations in the DFT functional. The quantum effects relevant at low temperatures may also be the source of the error. Nevertheless, our results at high temperatures are close to those of the experiments, which suggests that the method used in this work is promising in predicting isotope fractionations at high temperatures.

4.5. Implications for H isotope fractionation in subduction zone

Hydrogen isotope has been widely used to trace the water transported into the Earth's deep interior in the subduction zone (e.g., Shaw et al., 2008; 2012; Alt et al., 2012; Walowski et al., 2015; Dixon et al., 2017; Kuritani et al., 2021). The D/H isotope ratios of the subducting materials may change significantly with increasing depth due to the dehydration of hydrous minerals. Based on the experimentally determined isotope fractionation factors (e.g., Suzuoki and Epstein, 1976; Sakai and Tsutsumi, 1978; Graham et al., 1980; 1984; Saccocia et al., 2009) between fluids and the main hydrous phases in the slab lithologies, it is commonly accepted that the dehydration of the subducting materials would continuously release D-enriched fluids during subduction. The pressure effect on the D/H isotope fractionations between fluids and hydrous minerals is barely considered in recent studies. For example, Walowski et al. (2015) modeled the evolution of D/H isotope ratios of the released fluids during subduction to interpret the observed H isotope compositions of the melt inclusions from the Cascade Arc. They used the fluid-mineral isotope fractionation factors from the low-pressure experiments and ignored the pressure effect. However, the pressure effect on D/H isotope fractionations is found to be significant in the present work, the $10^3\ln(\alpha_H)$ value at 300 K increased from $-63.7‰$ at zero pressure to $-2.4‰$ at 3 GPa (Fig. 6a). Similarly, Horita et al., (2002) found that the $10^3\ln(\alpha_H)$ between brucite and water at 380 °C increased by $\sim$15‰ as pressure increased from 2.1 MPa to 800 MPa. The fractionations between other OH-bearing minerals (e.g., hornblende, serpentine, and epidote) and water would also be sensitive to the pressure, indicating that using the $10^3\ln(\alpha_H)$ values determined at low pressures to model the isotope fractionation between slab materials and fluids may have large errors. Thus, the D/H isotope ratios of the released fluids and the residue materials transported to the deep Earth may be completely different from what was thought before. Present work only provides the pressure dependence of $10^3\ln(\alpha_H)$ at a narrow situation (300 K, 0–3 GPa), systematic investigations of the pressure effect on the fluid-mineral fractionations are necessary to reveal the evolution of H isotope compositions of the fluids and slab materials during the subduction process.

5. Conclusion

This work determines the H and O isotope fractionation factors between brucite and water by PIMD simulations. The harmonic isotope fractionation factors are calculated for comparison. Based on the results, we find that the quantum effects are significant for both H and O in the two phases. The cancellation of the anharmonic effects has a large influence on the accuracy of the harmonic

Fig. 9. The PIMD and harmonic $^{18}O/^{16}O$ isotope fractionation factors (‰) between brucite and water. Previous experimental (Saccocia et al., 1998; 2015; Xu and Zheng, 1999) and theoretical (Zheng, 1998; Colla and Casey, 2019) results are presented for comparison.

isotope fractionations. The anharmonic effects on the RPFRs of brucite and water may be close to each other, the prerequisite is considering the temperature dependence of the volumes during harmonic calculations. The isotope fractionation factors predicted by PIMD-PBE simulations are significantly larger than the experimental values, this is because the PBE functional overestimates the proton excursion in the two phases. The results of PIMD-PBE0 are consistent with the results of the partial exchange experiments at high temperatures but distinct from those of the synthesis experiment at low temperatures. The discrepancies may be caused by the inaccuracy of the DFT functionals in predicting proton positions. The pressure effect on the H isotope fractionations is found to be significant at room temperature, whereas the O isotope fractionations are much less sensitive to the pressure change. Moreover, the H isotope fractionations between brucite and water have the trend to be inversed at high pressures, indicating that the H isotope fractionations between hydrous minerals and fluids in the deep Earth may be significantly different from those at near-surface conditions. This is important for investigations of water cycling into the deep Earth during the subduction process. The method used in this work generated acceptable isotope fractionation factors for brucite-water, especially at high temperatures. With the DP models, the isotope fractionations of the light elements among the condensed phases could be easily predicted by the PIMD simulations. The method is promising and has broad applications in the geoscience field.

Declaration of Competing Interest

The authors declare that they have no known competing financial interests or personal relationships that could have appeared to influence the work reported in this paper.

Acknowledgments

Appendix A. Supplementary material

The details of DBOC calculations and supplementary figures and tables can be found in Supplementary material 1. The research data associated with this article can be found in Supplementary material 2. The trained DP models can be found in Supplementary material 3. Supplementary materials to this article can be found online at https://doi.org/10.1016/j.gca.2023.02.004.

References

Adamo, C., Barone, V., 1999. Toward reliable density functional methods without adjustable parameters: The PBE0 model. J. Chem. Phys., 110

Alabaster, C.J., 1977. An occurrence of brucite at Merehead Quarry, Cranmore. Somerset. Mineral. Mag. 41, 406–408.

Alt, J.C., Garrido, C.J., Shanks, W.C., Turchyn, A., Padrón-Navarta, J.A., López Sánchez-Vizcaíno, V., Gómez Pugnaire, M.T., Marchesi, C., 2012. Recycling of water, carbon, and sulfur during subduction of serpentinites: A stable isotope study of Cerro del Almirez. Spain. Earth Planet. Sci. Lett. 327–328, 50–60.

Bartók, A.P., Payne, M.C., Kondor, R., Csányi, G., 2010. Gaussian Approximation Potentials: The Accuracy of Quantum Mechanics, without the Electrons. Phys. Rev. Lett. 104, 136403.

Behler, J., Parrinello, M., 2007. Generalized Neural-Network Representation of High-Dimensional Potential-Energy Surfaces. Phys. Rev. Lett. 98, 146401.

Bigeleisen, J., Mayer, M.G., 1947. Calculation of equilibrium constants for isotopic exchange reactions. J. Chem. Phys. 15, 261.

Born, K., Huang, K., 1956. Dynamical Theory of Crystal Lattices. Oxford University, New York.

Bowles, J.F.W., Howie, R.A., Vaughan, D.J., Zussman, J., 2011. Rock-forming minerals Vol. 5A – Non-silicates: oxides, hydroxides, and sulphides. The Geological Society, London, ISBN 978-1-86239-315-8, 920 pp.

Ceriotti, M., Parrinello, M., Markland, T.E., Manolopoulos, D.E., 2010. Efficient stochastic thermostatting of path integral molecular dynamics. J. Chem. Phys. 133, 124104.

Ceriotti, M., More, J., Manolopoulos, D.E., 2014. i-PI: A Python interface for ab initio path integral molecular dynamics simulations. Comp. Phys. Comm. 185, 1019–1026.

Ceriotti, M., Fang, W., Kusalik, P.G., McKenzie, R.H., Michaelides, A., Morales, M.A., Markland, T.E., 2016. Nuclear Quantum Effects in Water and Aqueous Systems: Experiment, Theory, and Current Challenges. Chem. Rev. 116 (13), 7529–7550.

Ceriotti, M., Markland, T.E., 2013. Efficient methods and practical guidelines for simulating isotope effects. J. Chem. Phys. 138, 014112.

Chakoumakos, B., Loong, C.K., Schultz, A., 1997. Low temperature structure and dynamics of brucite. J. Phys. Chem. B 101, 9458–9462.

Cheng, B., Ceriotti, M., 2014. Direct path integral estimators for isotope fractionation ratios. J. Chem. Phys. 141, 244112.

Chmiela, S., Tkatchenko, A., Sauceda, H.E., Poltavsky, I., Schütt, K.T., Müller, K.R., 2017. Machine learning of accurate energy-conserving molecular force fields. Sci Adv. e1603015.

Clayton, R.N., Goldsmith, J.R., Karel, K.J., Mayeda, T.K., Newton, R.C., 1975. Limits on the effect of pressure on isotopic fractionation. Geochim. Cosmochim. Acta 39, 1197–1201.

Colla, C.A., Casey, W.H., 2019. Calculated Oxygen-Isotope Fractionations among Brucite, Portlandite, and Water. ACS Earth Space Chem. 3, 1584–1593.

D'Antonio, M., Kristensen, M.B., 2004. Serpentine and brucite of ultramafic clasts from the South Chamorro Seamount (Ocean Drilling Program Leg 195, Site 1200): inferences for the serpentinization of the Mariana forearc mantle. Mineral. Mag. 68, 887–904.

Dawson, P., Hadfield, C., Wilkinson, G., 1973. The polarized infra-red and Raman spectra of $Mg(OH)_2$ and $Ca(OH)_2$. J. Phys. Chem. Solids 34, 1217–1225.

Dixon, J.E., Bindeman, I.N., Kingsley, R.H., Simons, K.K., Le Roux, P.J., Hajewski, T.R., Swart, P., Langmuir, C.H., Ryan, J.G., Walowski, K.J., Wada, I., Wallace, P.J., 2017. Light Stable Isotopic Compositions of Enriched Mantle Sources: Resolving the Dehydration Paradox. Geochem. Geophys. Geosyst. 18, 3801–3839.

Dupuis, R., Benoit, M., Nardin, E., Méheut, M., 2015. Fractionation of silicon isotopes in liquids: the importance of configurational disorder. Chem. Geol. 396, 239–254.

Dupuis, R., Benoit, M., Tuckerman, M.E., Méheut, M., 2017. Importance of a fully anharmonic treatment of equilibrium isotope fractionation properties of dissolved ionic species as evidenced by Li^+ (aq). Accounts Chem. Res. 50, 1597–1605.

Eldridge, D.L., Korol, R., Lloyd, M.K., Turner, A.C., Webb, M.A., Miller, T.F., Stolper, D.A., 2019. Comparison of Experimental vs Theoretical Abundances of $^{13}CH_3D$ and $^{12}CH_2D_2$ for Isotopically Equilibrated Systems from 1 to 500 °C. ACS Earth Space Chem. 3, 2747–2764.

Gao, C.H., Liu, Y., 2021. First-principles calculations of equilibrium bromine isotope fractionations. Geochim. Cosmochim. Acta 297, 65–81.

Gasparotto, P., Hassanali, A.A., Ceriotti, M., 2016. Probing Defects and Correlations in the Hydrogen-Bond Network of ab Initio Water. J. Chem. Theory Comput. 12, 1953–1964.

Goodfellow, I., Bengio, Y., Courville, A., 2016. Deep Learning. MIT Press.

Graham, C.M., Sheppard, S.M., Heaton, T.H., 1980. Experimental hydrogen isotope studies—I. Systematics of hydrogen isotope fractionation in the systems epidote-H_2O, zoisite-H_2O and AlO(OH)-H_2O. Geochim. Cosmochim. Acta 44 (2), 353–364.

Graham, C.M., Harmon, R.S., Sheppard, M.F., 1984. Experimental hydrogen isotope studies: hydrogen isotope exchange between amphibole and water. Am. Mineral. 69, 128–138.

Grimme, S., Ehrlich, S., Goerigk, L., 2011. Effect of the damping function in dispersion corrected density functional theory. J. Comp. Chem. 32, 1456.

Horita, J., Wesolowski, D.J., 1994. Liquid–vapor fractionation of oxygen and hydrogen isotopes of water from the freezing to the critical temperature. Geochim. Cosmochim. Acta 58, 3425–3437.

Horita, J., Cole, D.R., Wesolowski, D.J., 1999. Pressure effect on hydrogen isotope fractionation between brucite and water at elevated temperatures. Science 286, 1545–1547.

Horita, J., Cole, D.R., Polyakov, V.B., Driesner, T., 2002. Experimental and theoretical study of pressure effects on hydrogen isotope fractionation in the system brucite–water at elevated temperatures. Geochim. Cosmochim. Acta 66, 3769.

Horita, J., dos Santos, A.M., Tulk, C.A., Chakoumakos, B.C., Polyakov, V.B., 2010. High-pressure neutron diffraction study on H-D isotope effects in brucite. Phys. Chem. Mineral. 37, 741–749.

Horita, J., Driesner, T., Cole, D.R., 2018. Hydrogen isotope fractionation in the system brucite-water ± NaCl to elevated temperatures and pressures: Implications for the isotopic property of NaCl fluids under geologic conditions. Geochim. Cosmochim. Acta 235, 140–152.

Hostetler, P.B., Coleman, R.G., Mumpton, F.A., Evans, B.W., 1966. Brucite in alpine serpentinites. Am. Mineral. 51, 75–98.

Karandashev, K., Vaníček, J., 2017. Accelerating equilibrium isotope effect calculations: I. Stochastic thermodynamic integration with respect to mass. J. Chem. Phys., 146

Kell, G.S., 1977. Effect of isotopic composition, temperature, pressure, and dissolved gases on the density of liquid water. J. Phys. Chem. Ref. Data 6, 1109–1131.

Ko, H.-Y., Zhang, L., Santra, B., Wang, H., E W., DiStasio, Jr. R.A., Car, R., 2019. Isotope effects in liquid water via deep potential molecular dynamics. Mol. Phys. 117, 3269–3281.

Kresse, G., Furthmuller, J., 1996. Efficiency of ab-initio total energy calculations for metals and semiconductors using a plane-wave basis set. Comput. Mater. Sci. 6, 15–50.

Kuritani, T., Shimizu, K., Ushikubo, T., Xia, Q.-K., Liu, J., Nakagawa, M., Taniuchi, H., Sato, E., Doi, N., 2021. Tracing the subducting Pacific slab to the mantle transition zone with hydrogen isotopes. Sci. Rep. 11, 18755.

Liang, W., Lu, G., Yu, J., 2021. Theoretical prediction on the local structure and transport properties of molten alkali chlorides by deep potentials. J. Mater. Sci. Technol. 75, 78–85.

Liu, Q., Tossell, J.A., Liu, Y., 2010. On the proper use of the Bigeleisen-Mayer equation and corrections to it in the calculation of isotopic fractionation equilibrium constants. Geochim. Cosmochim. Acta 74, 6965–6983.

Lu, D., Jiang, W., Chen, Y., Zhang, L., Jia, W., Wang, H., Chen, M., 2022. DP Compress: A Model Compression Scheme for Generating Efficient Deep Potential Models. J. Chem. Theory Comput. 18, 5559–5567.

Luo, H., Karki, B.B., Ghosh, D.B., Bao, H., 2021a. Deep neural network potentials for diffusional lithium isotope fractionation in silicate melts. Geochim. Cosmochim. Acta 303, 38–50.

Luo, H., Karki, B.B., Ghosh, D.B., Bao, H., 2021b. Diffusional fractionation of helium isotopes in silicate melts. Geochem. Perspect. Let. 19, 19–22.

Luo, H., Karki, B.B., Ghosh, D.B., Bao, H., 2021c. Anomalous behavior of viscosity and electrical conductivity of MgSiO3 melt at mantle conditions. Geophys. Res. Let. 48. e2021GL093573.

Markland, T.E., Berne, B., 2012. Unraveling quantum mechanical effects in water using isotopic fractionation. Proc. Natl. Acad. Sci. USA 109, 7988–7991.

Markland, T.E., Ceriotti, M., 2018. Nuclear quantum effects enter the mainstream. Nat. Rev. Chem. 2, 0109.

Marsalek, O., Chen, P.Y., Dupuis, R., Benoit, M., Méheut, M., Bačić, Z., Tuckerman, M.E., 2014. Efficient calculation of free energy differences associated with isotopic substitution using path-integral molecular dynamics. J. Chem. Theory Comput. 10, 1440–1453.

Marsalek, O., Markland, T., 2015. Ab initio molecular dynamics with nuclear quantum effects at classical cost: Ring polymer contraction for density functional theory. J. Chem. Phys. 144, 054112.

Matsuhisa, Y., Goldsmith, J.R., Clayton, R.N., 1979. Oxygen isotopic fractionation in the system quartz-albite-anorthite-water. Geochim. Cosmochim. Acta 43, 1131–1140.

Matthews, A., Goldsmith, J.R., Clayton, R.N., 1983a. Oxygen isotope fractionations involving pyroxenes: The calibration of mineral- pair geothermometers. Geochim. Cosmochim. Acta 47, 631–644.

Matthews, A., Goldsmith, J.R., Clayton, R.N., 1983b. On the mechanisms and kinetics of oxygen isotope exchange in quartz and feldspars at elevated temperatures and pressures. Geol. Soc. Am. Bull. 94, 396–412.

Méheut, M., Lazzeri, M., Balan, E., Mauri, F., 2007. Equilibrium isotopic fractionation in the kaolinite, quartz, water system: Prediction from first-principles density-functional theory. Geochim. Cosmochim. Acta 71 (13), 3170–3181.

Méheut, M., Lazzeri, M., Balan, E., Mauri, F., 2010. First-principles calculation of H/D isotopic fractionation between hydrous minerals and water. Geochim. Cosmochim. Acta 74 (14), 3874–3882.

Nakajima, Y., Uchida, E., Imai, N., Imai, H., Ohno, H., 1992. Brucite-bearing white rock and the genetically related basalt dyke in the Nabeyama Carbonate Formation of the Kuzuu district, Tochigi Prefecture, Japan. J. Mineral. Petrol. Econ. Geol. 87, 445–459.

Neal, C., Stanger, G., 1984. Calcium and magnesium-hydroxide precipitation from alkaline groundwaters in Oman, and their significance to the process of serpentinization. Mineral. Mag. 48, 237–241.

Northrop, D.A., Clayton, R.N., 1966. Oxygen-isotope fractionations in systems containing dolomite. J. Geol. 74, 174–196.

Page, N.J., 1967. Serpentinization at Burro Mountain, California. Contr. Mineral. Petrol. 14, 321–342.

Perdew, J.P., Burke, K., Ernzerhof, M., 1996. Generalized gradient approximation made simple. Phys. Rev. Lett. 77, 3685–3868.

Pinilla, C., Blanchard, M., Balan, E., Ferlat, G., Vuilleumier, R., Mauri, F., 2014. Equilibrium isotope fractionation of H and O isotopes in water from path integral molecular dynamics. Geochim. Cosmochim. Acta 135, 203–216.

Pinilla, C., Blanchard, M., Balan, E., Natarajan, S.K., Vuilleumier, R., Mauri, F., 2015. Equilibrium magnesium isotope fractionation between aqueous Mg^{2+} and carbonate minerals: Insights from path integral molecular dynamics. Geochim. Cosmochim. Acta 163, 126–139.

Plimpton, S., 1995. Fast parallel algorithms for short-range molecular-dynamics. J. Comput. Phys. 117, 1–19.

Polyakov, V.B., 1998. On anharmonic and pressure corrections to the equilibrium isotopic constants for minerals. Geochim. Cosmochim. Acta 62 (18), 3077–3085.

Polyakov, V.B., Kharlashina, N.N., 1994. Effect of pressure on equilibrium isotopic fractionation. Geochim. Cosmochim. Acta 58, 4739–4750.

Polyakov, V.B., Horita, J., Cole, D.R., 2006. Pressure effects on the reduced partition function ratio for hydrogen isotopes in water. Geochim. Cosmochim. Acta 70, 1904–1913.

Praprotnik, M., Janežič, D., Mavri, J., 2004. Temperature dependence of water vibrational spectrum: A molecular dynamics simulation study. J. Phys. Chem. A 108, 11056–11062.

Redfern, S.A.T., Wood, B.J., 1992. Thermal expansion of brucite, $Mg(OH)_2$. Am. Mineral. 77, 1129–1132.

Reynard, B., Caracas, R., 2009. D/H isotopic fractionation between brucite $Mg(OH)_2$ and water from first-principles vibrational modeling. Chem. Geol. 262, 159–168.

Richet, P., Bottinga, Y., Javoy, M., 1977. A review of hydrogen, carbon, nitrogen, oxygen, sulphur, and chlorine stable isotope fractionation among gaseous molecules. Ann. Rev. Earth Planet. Sci. 5, 65–110.

Róg, T., Murzyn, K., Hinsen, K., Kneller, G.R., 2003. nMoldyn: A program package for a neutron scattering oriented analysis of molecular dynamics simulations. J. Comput. Chem. 24, 657–667.

Saccocia, P.J., Seewald, J.S., Shanks, W.C., 1998. Hydrogen and oxygen isotope fractionation between brucite and aqueous NaCl solutions from 250–450°C. Geochim. Cosmochim. Acta 62, 485–492.

Saccocia, P.J., Seewald, J.S., Shanks, W.C., 2009. Oxygen and hydrogen isotope fractionation in serpentine–water and talc–water systems from 250 to 450°C, 50MPa. Geochim. Cosmochim. Acta 73, 6789–6804.

Saccocia, P.J., Seewald, J.S., Shanks, W.C., 2015. Oxygen isotope fractionation in the portlandite–water and brucite–water systems from 125 to 450°C, 50MPa. Geochim. Cosmochim. Acta 169, 137–151.

Sakai, H., Tsutsumi, M., 1978. D/H fractionation factors between serpentine and water at 100 to 500 C and 2000 bar water pressure, and the D/H ratios of natural serpentines. Earth Planet. Sci. Lett. 40, 231–242.

Satake, H., Matsuo, S., 1984. Hydrogen isotopic fractionation factor between brucite and water in the temperature range from 100 to 510 °C. Contrib. Mineral. Petrol. 86, 19–24.

Schütt, K.T., Arbabzadah, F., Chmiela, S., Müller, K.R., Tkatchenko, A., 2017. Quantum-chemical insights from deep tensor neural networks. Nat. Commun. 8, 13890.

Shaw, A., Hauri, E., Fischer, T., Hilton, D., Kelley, K., 2008. Hydrogen isotopes in Mariana arc melt inclusions: Implications for subduction dehydration and the deep-Earth water cycle. Earth Planet. Sci. Lett. 275, 138–145.

Shaw, A., Hauri, E., Behn, M., Hilton, D., Macpherson, C., Sinton, J., 2012. Long-term preservation of slab signatures in the mantle inferred from hydrogen isotopes. Nature Geosci. 5, 224–228.

Soper, A.K., 2000. The radial distribution functions of water and ice from 220 to 673 K and at pressures up to 400 MPa. Chem. Phys. 258, 121–137.

Suzuoki, T., Epstein, S., 1976. Hydrogen isotope fractionation between OH-bearing minerals and water. Geochim. Cosmochim. Acta 40, 1229–1240.

Tilley, C.E., 1947. The gabbro-limestone contact zone of Camas Mor, Muck, Inverness-shire. Bull. Comm. Géol. Finlande 140, 97–105.

Trott, C.R., Hammond, S.D., Thompson, A.P., 2014. SNAP: Strong Scaling High Fidelity Molecular Dynamics Simulations on Leadership-Class Computing Platforms. Springer International Publishing, Cham, pp. 19–34.

Tuckerman, M., 2010. Statistical Mechanics: Theory and Molecular Simulation. Oxford University Press.

Turner, A.C., Korol, R., Eldridge, D.L., Bill, M., Conrad, M.E., Miller, T.F., Stolper, D.A., 2021. Experimental and theoretical determinations of hydrogen isotopic equilibrium in the system CH_4–H_2–H_2O from 3 to 200 °C. Geochim. Cosmochim. Acta 314, 223–269.

Urey, H.C., 1947. The thermodynamic properties of isotopic substances. J. Chem. Soc., 562–581

Vanicek, J., Miller, W., 2007. Efficient estimators for quantum instanton evaluation of the kinetic isotope effects: application to the intramolecular hydrogen transfer in pentadiene. J. Chem. Phys. 127, 114309.

Wagner, W., Pruβ, A., 2002. Thermodynamic properties of ordinary water. J. Chem. Ref. Data 31, 387–535.

Wagner, W., Riethmann, T., Feistel, R., Harvey, A.H., 2011. New Equations for the Sublimation Pressure and Melting Pressure of H2O Ice Ih. J. Phys. Chem. Ref. Data 40, 043103.

Walowski, K.J., Wallace, P.J., Hauri, E.H., Wada, I., Clynne, M.A., 2015. Slab melting beneath the Cascade Arc driven by dehydration of altered oceanic peridotite. Nature Geosci. 8, 404–408.

Wang, L., Ceriotti, M., Markland, T., 2014. Quantum fluctuations and isotope effects in ab initio descriptions of water. J. Chem. Phys. 141, 104502.

Wang, L., Ceriotti, M., Markland, T., 2020. Quantum kinetic energy and isotope fractionation in aqueous ionic solutions. Phys. Chem. Chem. Phys. 22, 10490–10499.

Wang, H., Zhang, L., Han, J., E W., 2018. DeePMD-kit: A deep learning package for many-body potential energy representation and molecular dynamics. Comput. Phys. Comm. 228, 178–184.

Webb, M.A., Miller, T.F., 2014. Position-specific and clumped stable isotope studies: comparison of the Urey and path-integral approaches for carbon dioxide, nitrous oxide, methane, and propane. J. Phys. Chem. A 118, 467–474.

Webb, M.A., Wang, Y., Braams, B.J., Bowman, J.M., Miller, T.F., 2017. Equilibrium clumped-isotope effects in doubly substituted isotopologues of ethane. Geochim. Cosmochim. Acta 197, 14–26.

Xu, N., Shi, Y., He, Y., Shao, Q., 2020. A Deep-Learning Potential for Crystalline and Amorphous Li–Si Alloys. J. Phys. Chem. C 124, 16278–16288.

Xu, B.L., Zheng, Y.F., 1999. Experimental studies of oxygen and hydrogen isotope fractionations between precipitated brucite and water at low temperatures. Geochim. Cosmochim. Acta 63, 2009–2018.

Zhang, L., Han, J., Wang, H., Car, R., E W., 2018. Deep Potential Molecular Dynamics: A Scalable Model with the Accuracy of Quantum Mechanics. Phys. Rev. Lett. 120, 143001.

Zhang, L., Wang, H., Car, R., E W., 2021. Phase diagram of a deep potential water model. Phys. Rev. Lett. 126, 236001.

Zhang, L., Lin, D.-Y., Wang, H., Car, R., Weinan, E., 2019. Active learning of uniformly accurate interatomic potentials for materials simulation. Phys. Rev. Mater. 3, 023804.

Zhang, Y., Liu, Y., 2018. The theory of equilibrium isotope fractionations for gaseous molecules under super-cold conditions. Geochim. Cosmochim. Acta 238, 123–149.

Zheng, Y.-F., 1998. Oxygen isotope fractionation between hydroxide minerals and water. Phys. Chem. Mineral. 25, 213–221.

Zhu, X., Guo, X., Smyth, J.R., Ye, Y., Wang, X., Liu, D., 2019. High-temperature vibrational spectra between $Mg(OH)_2$ and $Mg(OD)_2$: Anharmonic contribution to thermodynamics and D/H fractionation for brucite. J. Geophys. Res. Solid Earth 124, 8267–8280.

Zimmermann, T., Vanicek, J., 2009. Path integral evaluation of equilibrium isotope effects. J. Chem. Phys. 131, 024111.